Materials Advances

ROYAL SOCIETY OF CHEMISTRY

PAPER

View Article Online
View Journal | View Issue

Cite this: *Mater. Adv.*, 2025, 6, 9723

Hierarchical integration of a MoS_2 nanoflower/MnO_2 nanorod/CNT ternary composite electrode for high capacitance and long-term cycling stability

Md. Arif Hossain Chowdhury Anik, †[a] T. M. A. Iqbal Bin Belal, †[a] Md Shafayatul Islam,[ab] Koushik Roy Chowdhury,[a] Mrinmoy Brahma,[a] Shad Inquiad Mim,[c] Aninda Nafis Ahmed*[c] and Ahmed Sharif *[a]

MoS_2 nanoflowers, with their high surface area and substantial number of active sites in the layered structure, are promising candidates for charge storage. However, their poor electrical conductivity, severe sheet restacking, and cycling-induced degradation significantly hinder their rate capability and long-term stability. To overcome these limitations, MnO_2 nanorods that possess pronounced pseudocapacitance are incorporated to provide complementary redox active sites and improve overall electrochemical performance. However, MnO_2 nanorods suffer from volumetric fluctuations and sluggish charge transport, leading to rapid capacitance decay at elevated current densities. Introducing CNTs overcomes many of these challenges by forming a highly conductive, flexible network that improves electron transport and structural stability, synergistically boosting the performance of the MoS_2/MnO_2 composite to function as a supercapacitor electrode material. High performance supercapacitors require electrode materials that unify high capacitance, conductivity, and stability; such features are seldom found in a single component. Therefore, in this work, we first fabricated MoS_2/MnO_2 binary composites with varying MnO_2 content and subsequently introduced 1 wt% CNTs into the optimized binary system to develop a MoS_2/MnO_2/CNT ternary composite *via* a facile hydrothermal route. The MoS_2/MnO_2/CNT composite offers numerous active sites and enhanced redox activity while ensuring rapid ion transfer efficiency to boost pseudocapacitance performance. Electrochemical characterization, performed in a 1 M KOH electrolyte, demonstrated that the MoS_2/MnO_2 (5 wt%)/CNT (1 wt%) electrode achieved a remarkable specific capacitance of 457 F g^{-1} at 0.15 A g^{-1} and retained 96% capacity with 100% coulombic efficiency over 2000 cycles. Notably, it delivers an energy density of 37 Wh kg^{-1} while maintaining excellent electrochemical stability and performance integrity. The synergistic interaction between the constituent components yields a defect-rich structure with high conductivity, structural stability, low charge transfer resistance, and improved cycling durability establishing the composite as a compelling candidate for advanced energy storage and seamless renewable energy integration.

Received 28th July 2025,
Accepted 23rd October 2025

DOI: 10.1039/d5ma00817d

rsc.li/materials-advances

1. Introduction

The world's energy crisis is getting severe as we use up more of our fossil fuels, harm the environment, and lose the balance of nature that we all depend on. Renewable energy sources including solar, wind, and hydropower are being used more frequently to decrease emissions of greenhouse gases and the consumption of fossil fuels. However, due to their dependence on local weather and climate, these renewable energy sources cannot guarantee a consistent supply. This makes it essential to have safe, cheap, and stable energy storage systems that work well. Energy storage systems store additional power and release it when needed, therefore ensuring a continuous power supply.[1] Among these energy storage systems, capacitors store energy electrostatically by separating opposing charges on plates without incurring any chemical changes. Batteries, on the other hand, store energy through redox chemical processes.

[a] *Department of Materials and Metallurgical Engineering, Bangladesh University of Engineering and Technology, Dhaka 1000, Bangladesh. E-mail: asharif@mme.buet.ac.bd*
[b] *Department of Materials Science and Engineering, University of Illinois Urbana Champaign, Urbana, Illinois, 61801, USA*
[c] *Pilot Plant and Process Development Centre, Bangladesh Council of Scientific and Industrial Research, Dhaka, Bangladesh. E-mail: adhi88bd@yahoo.com*
† Md. Arif Hossain Chowdhury Anik and T. M. A. Iqbal Bin Belal contributed equally to this work.

Capacitors can undergo millions of cycles, but they only achieve high energy density when they are enormous. Supercapacitors (SCs) are gaining attention for their eco-friendliness, long cycle life, fast-discharge, and high-power density, making them ideal to bridge batteries and traditional capacitors. However, their energy density is still lower than batteries. To enhance performance, researchers combine carbon materials with pseudocapacitive oxides or sulfides.

MoS_2, a layered transition metal dichalcogenide, is often used for its charge storage ability but typically requires conductive additives. MoS_2 is made up of two-dimensional layers that are connected by S–Mo–S bonds.[2] The Mo atoms have different valence states (+2 to +6) and MoS_2 contains a large specific surface area and porous structure. This configuration provides numerous active sites for interaction with electrolyte ions, which gives it its pseudocapacitance property. But MoS_2 layers often break down during cycling due to irreversible phase changes and lattice strain.[3] These issues reduce the stability and reliability of MoS_2 based supercapacitors. Despite its low energy density, it is often combined with conductive materials to enhance its conductivity.[4,5] Recently, combining metal oxides with MoS_2 enhances energy storage in supercapacitors to overcome these limitations.[6] Scientists have constructed heterostructures from materials like MnO_2 to tackle this problem, therefore enhancing the electron flow and supercapacitor efficiency.[7,8] MnO_2 is a low-cost, non-toxic pseudocapacitive material with high theoretical capacitance ($\sim$1370 F g^{-1}) and works well with neutral aqueous electrolytes. Its fast redox reactions, surface cation exchange, and large tunnel structure enable both faradaic and double-layer capacitance, allowing rapid ion transport and fast charge–discharge rates.[9] However, MnO_2 has low electrical conductivity (10^{-5}–10^{-6} S cm^{-1}), which makes it much less effective at storing charge and performing at high speed.[10,11] But if the MnO_2 load is too much, it can clog ionic channels, which makes the performance worse again.[12,13] MoS_2 and MnO_2 both have low intrinsic conductivity, which makes it difficult for electrons to move quickly in pseudocapacitive reactions.[14,15] When these materials are in their nanostructured form, they also tend to clump together or restack. This phenomenon makes their active surface area smaller and blocks ion pathways.[16] Additionally, these materials are mechanically unstable during repeated charge and discharge cycles due to changes in their volume, which negatively impacts long-term cycling stability.

Combining CNTs solves many of these limitations.[12,17] Carbon nanotubes (CNTs) excel as supercapacitor electrode materials due to their metal-like conductivity, high surface area, and robust mechanical strength. Their one-dimensional sp^2 framework allows ultrafast electron transport, significantly reducing internal resistance and raising the power density.[13] They help the electrode keep its shape and work well for many cycles. They prevent MoS_2 and MnO_2 from sticking, improve electrolyte access, and accommodate volume changes.[18,19] Many studies show that MoS_2/CNT and MnO_2/CNT composites have much better conductivity, lower impedance, better capacitance retention, and better rate capability than pure MoS_2 or MnO_2 systems.[20] Chen *et al.*[21] synthesized a MoS_2/CNT composite using a simple hydrothermal method, achieving 402 F g^{-1} at 1 A g^{-1} and retaining 81.9% capacitance after 10 000 cycles. Sahoo *et al.*[22] synthesized a MoS_2/MnO_2 composite by combining liquid-exfoliated MoS_2 nanosheets with hydrothermally prepared MnO_2 nanowires, achieving a specific capacitance of 212 F g^{-1} at 0.8 A g^{-1} and retaining 84.1% after 5000 charge–discharge cycles. Various methods like nano structuring, composites, and surface modification have improved MoS_2-based electrodes. However, the electrochemical behavior of MoS_2 nanoflowers combined with 1D MnO_2 nanorods and CNTs, especially with varying MnO_2 content, remains unexplored.[4] In this project, we prepared MnO_2 nanorod and CNT-incorporated MoS_2 nanoflower nanocomposites *via* a simple hydrothermal method. We fabricated binary nanocomposites of MoS_2 nanoflower with MnO_2 (3 wt%, 5 wt%) and a ternary nanocomposite by adding CNT (1 wt%) to the binary composite. Electrochemical tests in 1 M KOH using a three-electrode setup showed that the MoS_2/MnO_2/CNT electrode had the highest specific capacitance of around 457 F g^{-1} at a current density of 0.15 A g^{-1}. The composite also showed excellent stability, retaining about 96% of its initial capacitance over 2000 charge–discharge cycles. This surpasses many previous reports. Moreover, the ternary nanocomposite achieved an energy density of $\sim$37 Wh kg^{-1}, without affecting the cyclic life. In the case of the MoS_2/MnO_2/CNT electrode, MoS_2 provides a large surface area and easy ion movement for better energy storage.[23] MnO_2 nanorods exhibit pseudocapacitance through rapid redox reactions, and their tunnel structure enables quick ion insertion and extraction, supporting fast charge discharge rates and structural support.[24] Conversely, carbon nanotubes (CNTs) form a very conductive network that increases electron transportation, prevents materials from sticking, and imparts flexible properties to the structure.[10] This carefully engineered composite might effectively enhance outstanding throughput, superior capacitance, and long-term stability by harnessing the finest qualities of each component while skillfully overcoming the limitations of MoS_2 and MnO_2. Thus, these synergistic features establish this supercapacitor electrode as a promising candidate for a high-performance energy storage system by enabling seamless integration of renewable sources.

2. Material synthesis

2.1. Materials

All chemical reagents employed in this investigation were of analytical quality and used without additional purification. During the entire experiment, deionized (DI) water with a resistivity of 18.2 MΩ cm was utilized. Manganese sulfate monohydrate ($MnSO_4{\cdot}H_2O$), dimethyl sulfoxide (C_2H_6OS), polyvinyl alcohol (PVA), potassium hydroxide (KOH), and aqueous thiourea (NH_2CSNH_2) were obtained from Research Lab, India. Potassium permanganate ($KMnO_4$) was purchased from Alpha Chemicals, India. Sodium molybdate dihydrate ($Na_2MoO_4{\cdot}2H_2O$) and ethanol (C_2H_6O) were procured from Merck, Germany. Carbon nanotubes (MWCNTs) of length 10–30 μm

and outer diameter 5–15 nm with 99% purity were collected from XFNANO.

2.2. Preparation of MnO_2 nanorods

The desired MnO_2 nanorods were prepared by using a facile hydrothermal approach. Subsequently, 2.8439 g of $MnSO_4{\cdot}H_2O$ and 1.1829 g of $KMnO_4$ were accurately weighed and dissolved in 60 mL of deionized water, followed by vigorous stirring for 40 minutes to obtain a purple solution. The solution was shifted to a 120 mL Teflon-lined autoclave and heated at 140 °C for 12 hours in an electric furnace. When the furnace cooled down to room temperature, the brown precipitate that formed was carefully collected, washed multiple times with deionized water and ethanol, and dried at 80 °C for several hours. Finally, a brown MnO_2 nanorod powder was obtained.[25]

2.3. Preparation of MoS_2 nanoflowers

2.035 g of sodium molybdate dihydrate ($Na_2MoO_4{\cdot}2H_2O$) and 2.87 g of thiourea (CH_4N_2S) were weighed and dissolved in 60 mL of deionized water with vigorous stirring for 45 minutes to form a clear solution. After that, the solution was placed in an autoclave that was lined with Teflon and heated up in a furnace at 180 °C for 24 hours. The black precipitate was collected once the furnace cooled down to room temperature. It was then washed multiple times with deionized water and ethanol and dried at 60 °C for a few hours. Finally, a black MoS_2 nanoflower powder was obtained.[26,27]

2.4. Preparation of the MoS_2/MnO_2 nanocomposites

For this work, MoS_2/MnO_2 nanocomposites were synthesized with 3 wt% and 5 wt% MnO_2. To prepare the 3 wt% composite, the desired amount of MnO_2 nanorods was dispersed in 20 mL of deionized water and sonicated for 1 hour. Separately, 2.035 g of sodium molybdate dihydrate ($Na_2MoO_4{\cdot}2H_2O$) and 2.87 g of thiourea (CH_4N_2S) were dissolved in 60 mL of deionized water and stirred for 45 minutes until a clear solution formed. After that, this mixture was added to the MnO_2 suspension and mixed for a further hour. The mixture was then placed into an autoclave that was lined with Teflon and heated at 180 °C for 24 hours. After being cooled to room temperature the black precipitate was then washed multiple times with ethanol and deionized water. The precipitate was dried at 80 °C for a few hours. The final product was MnO_2-incorporated MoS_2 nanoflowers. The same procedure was followed for the 5 wt% MnO_2 composite.

2.5. Preparation of the MoS_2/MnO_2/CNT nanocomposite

For this work, the MoS_2/MnO_2/CNT nanocomposite was synthesized by adding the precursor solution of MoS_2 into 5 wt% MnO_2 and 1 wt% CNT dispersion. To prepare the 5 wt% composite, the desired amount of MnO_2 nanorods was dispersed in 20 mL of deionized water and sonicated for 1 hour. Similarly, the required amount of CNTs was dispersed in 10 mL of deionized water and sonicated for 1 hour, following the same procedure as MnO_2. After that, the sonicated CNT mixture was added to the MnO_2 dispersion. Separately, 2.035 g of sodium molybdate dihydrate ($Na_2MoO_4{\cdot}2H_2O$) and 2.87 g of thiourea (CH_4N_2S) were dissolved in 50 mL of deionized water and stirred for 45 minutes until a clear solution formed. This solution was then added to the MnO_2/CNT dispersion and stirred for another hour. After that, the mixture was moved into an autoclave that was lined with Teflon and heated at 180 °C for 24 hours. After being cooled down to room temperature the black precipitate was then washed multiple times with ethanol and deionized water. The precipitate was dried at 80 °C for several hours. The final product was MnO_2 and CNT-incorporated MoS_2 nanoflowers. The synthesis route is presented in Fig. 1.

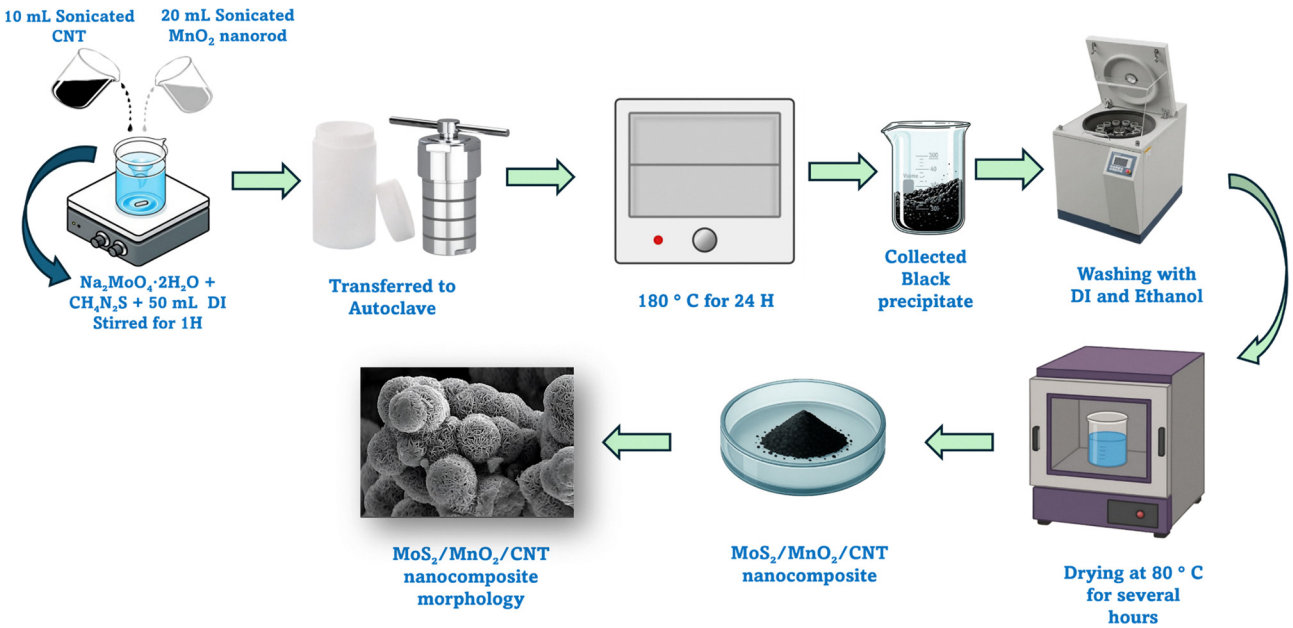

Fig. 1 Schematic diagram of the synthesis of the MoS_2/MnO_2/CNT composite through a hydrothermal route.

2.6. Materials' characterization

The Empyrean diffractometer was used at room temperature with Cu Kα radiation (λ = 1.5406 Å) and scanned at a rate of 5° per minute to study the crystal structures of the samples through X-ray diffraction (XRD). The surface chemical states and elemental composition were investigated by employing X-ray photoelectron spectroscopy (XPS) with monochromatic Al Kα radiation on a Thermo Fisher Scientific Escalab Xi+ equipment. To determine the chemical structures and functional groups of the materials, we employed Fourier-transform infrared (FTIR) spectroscopy with a Japanese Miyazaki IRSpirit-T. Scanning electron microscopy (Tescan Vega Compact) was used to analyze the surface morphology and intricate structural characteristics. To improve the interpretation of the SEM images, they were further examined using ImageJ software. To identify elements and their amounts in the samples, energy dispersive X-ray spectroscopy (EDX) was employed.

2.7. Electrode preparation

A uniform slurry was prepared by mixing the synthesized sample powder with dimethyl sulfoxide (DMSO) as the solvent and polyvinyl alcohol (PVA) as the binder. The amount of PVA used was 5 wt% relative to the active material. This slurry was thoroughly sonicated for 1 hour to ensure proper mixing. The slurry was then evenly coated onto a graphite rod surface (0.4 cm^2). The mass of the electrode material was calculated by measuring the weight of the electrode before and after coating. PVA was chosen as the binder because its multiple hydroxyl groups can form

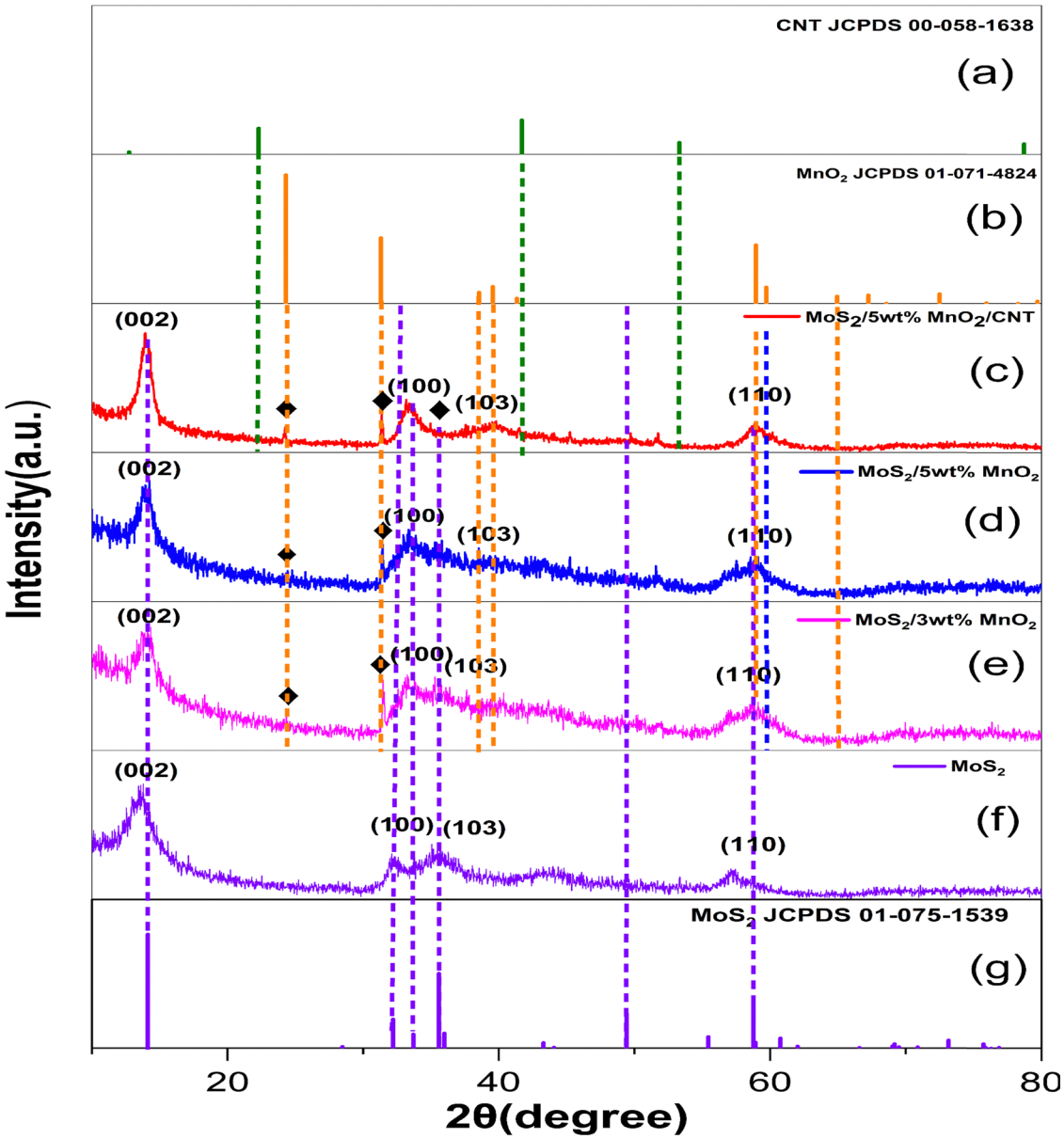

Fig. 2 XRD patterns of (a) CNT JCPDS 00-058-1638, (b) MnO_2 JCPDS 01-071-4824, (c) MoS_2/MnO_2 (5 wt%)/CNT (1 wt%), (d) the MoS_2/MnO_2 (5 wt%) composite, (e) MoS_2/MnO_2 (3 wt%), (f) pristine MoS_2, and (g) MoS_2 JCPDS 01-075-1539.

strong hydrogen bonds with both the active material and the current collector. It also provides excellent adhesion for high-performance electrodes.[28,29] After coating, the electrodes were dried at 60 °C for several hours before being used as working electrodes in electrochemical tests.

2.8. Electrochemical measurements

The Gamry Instruments Reference 3000, an electrochemical workstation with a standard three electrode configuration, was employed to evaluate the electrochemical performance of the prepared materials. The working electrode was a graphite rod onto which the synthesized sample was deposited. The reference electrode was an Ag/AgCl electrode, while the counter electrode was platinum. Electrochemical impedance spectroscopy (EIS), cyclic voltammetry (CV), galvanostatic charge discharge (GCD) experiments, and cycling stability in a 1 M potassium hydroxide (KOH) solution were employed to investigate electrochemical behavior. All measurements were conducted within a potential window of −0.4 to 0.4 V *vs.* Ag/AgCl. The EIS was performed by administering a sinusoidal voltage within a frequency range of 0.1 Hz to 10^6 Hz.

3. Results and discussion

3.1. X-ray diffraction

To verify the crystal structure, phase purity, and crystallinity of the synthesized composite, XRD analysis was performed at room temperature with anode material Cu, with Kα = 1.54 Å, X-rays generated at 40 mA and 45 kV. Fig. 2(c–f) represents XRD patterns of the ternary nanocomposite of MoS_2/MnO_2/CNT, MoS_2/MnO_2 composites with varying MnO_2 content and pristine MoS_2. Observing the diffraction patterns of pristine MoS_2 in Fig. 2(f), the most prominent peak was found at a 2θ value of approximately 14.4° for the (002) plane reflection. This peak corresponds to the interlayer spacing of the MoS_2 nanosheets making the nanoflower petals. During synthesis, layered MoS_2 develops well stacked along the *c* axis, as a result of which a sharp peak at 14.4° is seen.[30] Other significant peaks were found at 33.1° (100), 39.5° (103), 49.8° (105), and 58.3° (110). These peaks are in excellent agreement with the reference pattern (JCPDS No. 01-075-1539) shown in Fig. 2(g). The diffraction peaks of the synthesized pristine MoS_2 thus confirmed to be matched with the hexagonal crystal system of MoS_2-2H (Fig. S5a).

The diffraction peaks of the synthesized MnO_2 exhibited main reflections at around 28.7° (110), 37.3° (101), 42.8° (111), and 56.7° (211). Upon introducing the MnO_2 nanorods, the XRD patterns of the binary composites, MoS_2/MnO_2 (3 wt%) (Fig. 2e) and MoS_2/MnO_2 (5 wt%) (Fig. 2d), clearly show the retention of the MoS_2 host structure. Concurrently, new diffraction peaks, marked by the diamond symbol (♦), appear at approximately 26.5° and 32.5°. These peaks correspond to the (110) and (111) planes of the tetragonal β-MnO_2 phase, confirming the successful incorporation of crystalline MnO_2 nanorods (JCPDS No. 01-071-4824) shown in Fig. 2(b). The XRD pattern for pure MnO_2 is shown in Fig. S1. As the fraction of MnO_2 is increased, the peak of MnO_2 becomes prominent. The peak positions of the MoS_2 nanoflowers are slightly changed, which suggests that the MnO_2 nanorods are causing lattice distortion or intercalation.[3] The diffraction pattern of the ternary composite in Fig. 2(c) shows the presence of peaks at 24.3°, 32°, and 59° corresponding to the planes of (110), (220), and (330) indicating the presence of MnO_2 in the composite. The composite XRD spectrum displays characteristic diffraction peaks that correspond to each individual component. As CNT was added at only 1 wt%, the characteristic peak intensity was found to be very low. The low intensity of the CNT peak is attributed to the high dispersion of the CNTs within the matrix and a potential shielding effect from the more crystalline and higher mass components.

A very low intense diffraction peak centered at approximately 26°, which is attributed to the (002) plane of amorphous carbon. Another weak peak is observed around 43°, corresponding to the (100) plane of carbon. The broadness of these peaks is attributed to the nano-crystalline size and the cylindrical nature of the nanotubes.[31] Thus, the XRD pattern of the final hierarchical nanocomposite, MoS_2/MnO_2 (5 wt%)/CNT (1 wt%) shown in Fig. 2(c), validates the successful assembly of all three nanoscale components. The pattern is a definitive superposition of the constituent phases. The resulting material is not simply nanocrystalline; it is a highly strained, defect-rich system with crystalline domains so small and distorted that its properties may begin to approach those of a disordered or quasi-amorphous material.[32] For quantitative analysis, the crystallite size (L), the density of dislocation (δ), and the microstrain (ε) of all samples were determined from the (002) peak using eqn (1)–(3):

$$\varepsilon = \frac{\beta}{4\tan\theta} \quad (1)$$

$$\delta = \frac{1}{L^2} \quad (2)$$

where λ = X-ray wavelength, θ = diffraction angle, and β = diffraction peak FWHM. The results are summarized in Table 1. The constituent phases, instrument operating parameters, corresponding JCPDS cards, and degree of crystallinity (%) are summarized in Table S1.

Quantitative analysis shows that when the MnO_2 content goes up, the average size of the MoS_2 nanoflowers gets smaller and the crystallite size was the lowest for the ternary composite, as seen in Fig. 3(c). The MnO_2 nanorods and CNTs effectively prevent the MoS_2 from forming large, well-ordered crystalline domains. The MnO_2 nanorods and CNTs act as heterogeneous nucleation sites that simultaneously promote the formation of MoS_2 but restrict its ability to achieve high crystallinity. This process leads directly to the formation of many small, disordered crystallites rather than a few large ones, explaining the observed reduction in crystallite size. Smaller grains increase boundary density, shorten ion diffusion lengths, and expose more active edge sites for faster ion/electron kinetics.[33,34]

Concurrent with the reduction in crystallite size, the density of defects within the MoS_2 lattice shown in Fig. 3(b) increases

Table 1 Diffraction parameters of synthesized samples obtained from XRD analysis

Samples	L (nm)	d(002) (Å)	d(001) (Å)	$a = b$ (Å)	c (Å)	Micro strain, $\varepsilon \times 10^{-3}$	$\delta \times 10^{-3}$ (nm^{-2})
MoS_2	6.25	6.42	2.775	3.204	12.84	39.68	25.60
MoS_2/MnO_2 (3 wt%)	5.88	6.39	2.773	3.201	12.78	47.84	28.92
MoS_2/MnO_2 (5 wt%)	5.71	6.45	2.779	3.208	12.92	49.25	30.67
MoS_2/MnO_2 (5 wt%)/CNT (1 wt%)	5.51	6.47	2.781	3.211	12.96	51.03	32.93

significantly.[35] Table 1 reveals that the dislocation density within the MoS_2 structure rises as more MnO_2 is added and it was the highest for the ternary composite. This is accompanied by an increase in the internal micro-strain shown in Fig. 3(a). The main reason for this phenomenon is the difference in the arrangement of atoms between the crystal structure of the MnO_2 nanorods (like β-MnO_2) and the MoS_2 nano petals (hexagonal 2H-MoS_2).[36] Elevated lattice strain and increased dislocation density generate defect-rich regions with abundant grain boundaries and imperfections, serving as additional electroactive sites that enhance ion adsorption, charge storage, and redox activity, which are critical for high performance supercapacitor electrode materials.[16]

The absence of any impurity peaks highlights the high phase purity of the product. The nanocrystalline nature, confirmed by peak broadening, combined with the integration of these distinct 1D (nanorods, nanotubes) and 3D (nanoflowers) morphologies, suggests the formation of a complex and high surface area containing ideal material for advanced energy storage applications.

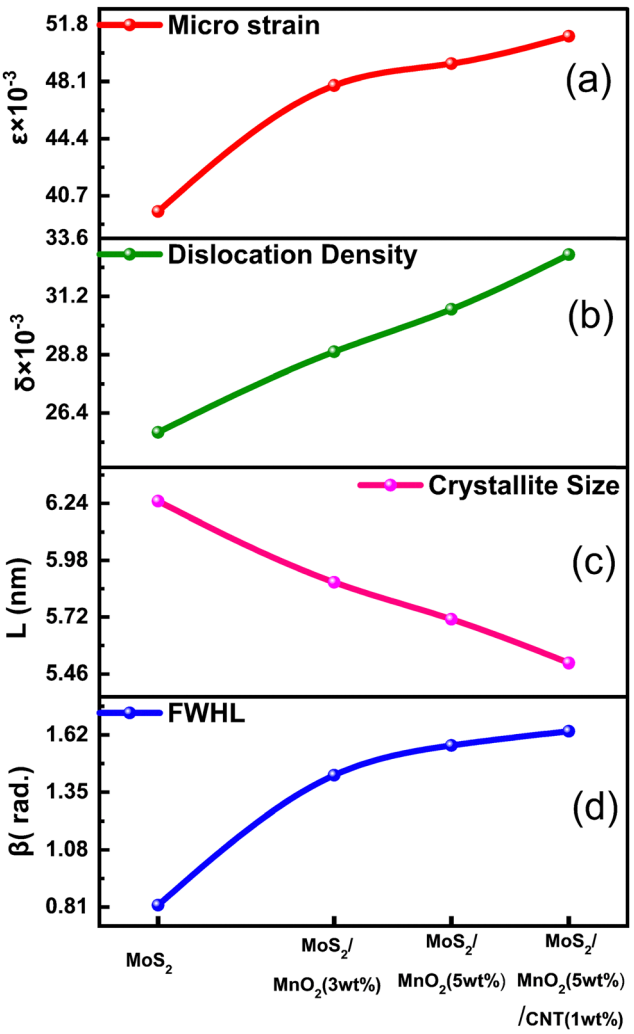

Fig. 3 Variation of (a) micro strain (ε), (b) dislocation density (δ), (c) crystallite size (L), and (d) FWHM(β) for the MoS_2 nanoflower, MoS_2/MnO_2 (3 wt%), MoS_2/MnO_2 (5 wt%) and MoS_2/MnO_2 (5 wt%)/CNT (1 wt%) nanocomposites, respectively.

3.2. Scanning electron microscopy

The synthesized MoS_2/MnO_2/CNT composites were analyzed through a scanning electron microscope to observe the surface morphology, nanostructure, and distribution of components in the composite to confirm successful synthesis. The correlation of electrochemical performance with the structural features was also studied. Fig. 4(c) represents the SEM image of MoS_2 NF. The SEM image shows a 3D nanostructure resembling a flower-like morphology with multiple petals radiating from central cores. This kind of feature maximizes surface exposure while maintaining structural integrity. The average diameter of the MoS_2 NFs is around 4–6 μm. A shared core center connects several MoS_2 nano petals of average length 1–1.2 μm. The petal thickness was found to be between 20–40 nm. MoS_2 nanoflowers form stable, porous, flower-like clusters that expose many active edge sites and boost both EDLC and pseudocapacitance. They also provide a rigid 3D scaffold that resists collapse during cyclic charge discharge.[37] The synthesis of the MoS_2 NF through the hydrothermal route may involve the following reaction:

$$Na_2MoO_4{\cdot}2H_2O + CH_4N_2S \rightarrow MoS_2 + CO(NH_2)_2 + Na_2SO_4 + 4H_2O \quad (4)$$

Fig. 4(a) represents the SEM images of MnO_2 nanorods. The lengths of these rods range from 1–3 μm and diameters range from 60 to 98 nm. Fig. S3(b) shows that the nanorods have a smooth surface under high magnification.[38] MnO_2 nanorods act as spacers and conductive bridges. It also prevents MoS_2 agglomeration and shortens ion/electron pathways. Embedding these flowers in MnO_2 nanorods and a CNT network creates a three-dimensional charge-transfer network and electrolyte diffusion channels. Some MnO_2 nanorods exhibit broken edges because their growth was not fully complete during synthesis. The surface of these rods boosts the composite's electrochemical performance by increasing the overall surface area and exposing more electroactive and metal active sites. As an extra benefit, the rods may form many new

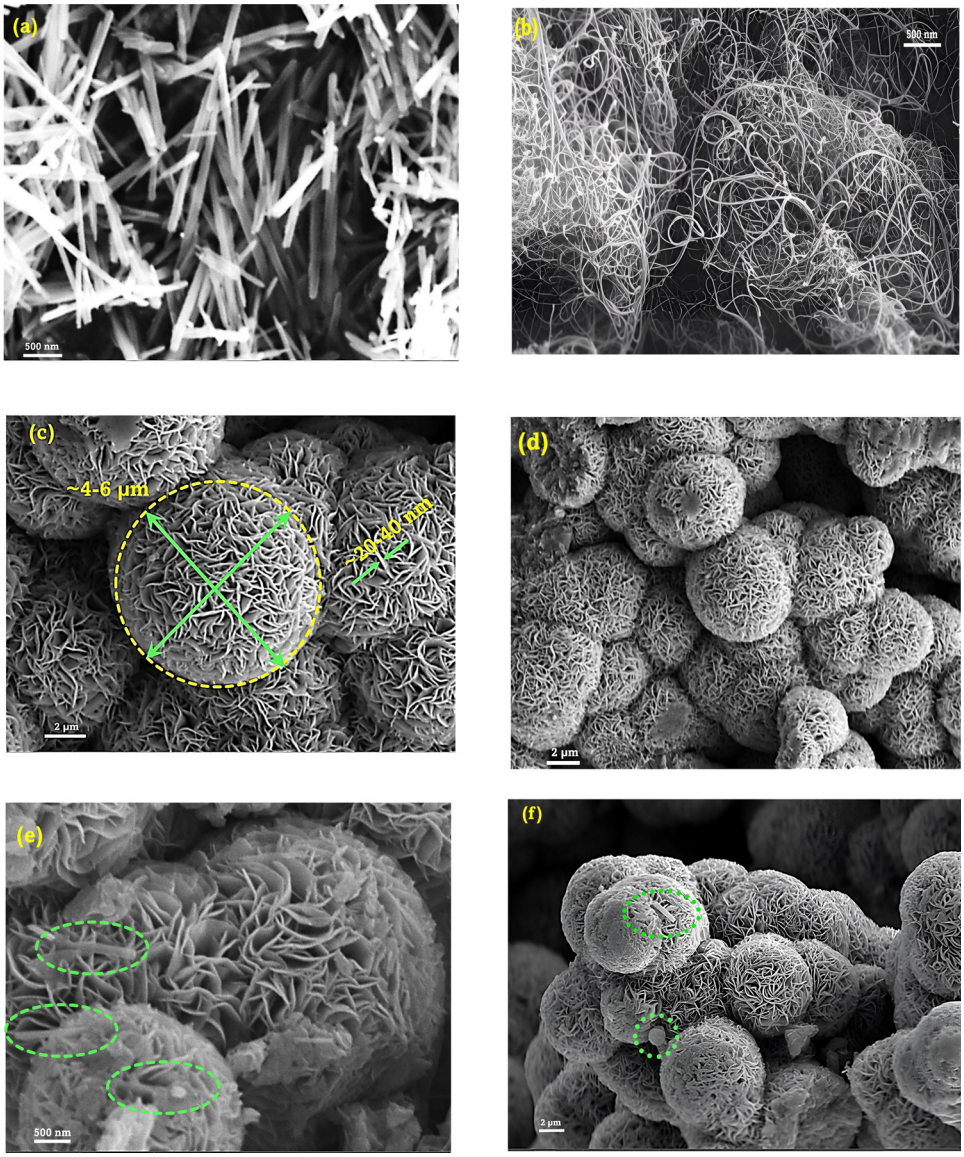

Fig. 4 (a) and (b) SEM images of MnO_2 nanorods and CNTs, respectively; (c)–(f) SEM images of the MoS_2 nanoflower, MoS_2/MnO_2 (3 wt%), MoS_2/MnO_2 (5 wt%) and MoS_2/MnO_2 (5 wt%)/CNT (1 wt%) nanocomposites, respectively.

channels and pathways. These pathways help ions move and accumulate more easily. The synthesis of the MnO_2 nanorod through the hydrothermal route may involve the following reaction:

$$3MnSO_4 + 2KMnO_4 + 2H_2O \rightarrow 5MnO_2 + K_2SO_4 + 2H_2SO_4 \quad (5)$$

where Mn^{2+} is oxidized, $KMnO_4$ is reduced, and β-MnO_2 precipitates as nanorods. Fig. 4(b) represents the SEM of multi-walled carbon nanotubes (MWCNTs). The tubes are elongated, hollow cylindrical nano objects with outer diameters ranging from 15–20 nm and lengths extending from hundreds of nm to several μm. The wall thickness remains fairly constant along the nanotube axis, creating a straight inner channel. Fig. S3(a) reveals that MWCNTs have a strong tendency to bundle together due to van der Waals intermolecular forces. These bundles form netlike nanostructures where individual nanotubes are interconnected. The CNT scaffold also buffers the collapse and aggregation of active materials during charge discharge. CNTs boost electrical conductivity by orders of magnitude. It also prevents restacking and accessible surface area by lowering charge-transfer resistance.[21]

In Fig. 4(d–f) the SEM images of the MoS_2/MnO_2 (3 wt%), MoS_2/MnO_2 (5 wt%) and MoS_2/MnO_2 (5 wt%)/CNT (1 wt%) nanocomposites are shown, respectively. Due to the addition of precursors of MoS_2 in hot water, small MoS_2 nuclei initially form and adhere to the MnO_2 and CNT. As the space around the rods and fibers pushes them outward, the nuclei expand into layered sheets. These sheets grow and stack on top of each other, like petals on a flower, until they look like a ''nanoflower''. The 3D structure is held together by strong bonds such as van der Waals, cohesive, electrostatic or other chemical forces at the surface when the MnO_2 nanorod and CNT were

dispersed in the solution.[39] The curved petals of the MoS_2 are more homogeneous and neatly aligned. They seem to be tightly attached to the core, indicating that the MnO_2 nanorod served as a backbone and the CNT worked as a scaffold. The discovered nanoflowers have diameters ranging from 4 to 6 μm and either form clusters or are independent of one another.[40] The diameter of the MoS_2 nanoflower gets smaller with increasing MnO_2 concentration and was smallest in the MoS_2/MnO_2/CNT composite. Due to the increase in MnO_2 and the addition of CNT, more nucleation sites are added, and they physically restrict MoS_2 growth. That results in smaller nanosheets and ultimately smaller nanoflowers.[41] Fig. 4(f) shows that the presence of CNT is not clearly visible because of the low concentration. However, its presence was confirmed in the composite by analyzing the EDX in different regions. The elemental distribution of Mo, S, Mn, O, and C was also examined. EDX analysis also verified that the nanorods contain Mn and O, the nanoflowers consist of Mo and S, and the binary and ternary composites contain the constituent elements shown in Fig. S2(a–d). By analyzing the EDX, it was observed that the atomic Mo to S ratio is greater than the ideal MoS_2 stoichiometry (1 : 2). Therefore, it is evident that the MoS_2/MnO_2/CNT nanocomposites are rich in sulfur. This excess sulfur likely indicates a high density of structural defects, particularly sulfur vacancies or sulfur adatoms. These defects help lower the surface energy and make the ultrathin sheets more stable. They create a high number of reactive sites, especially at sulfur vacancy locations, which dramatically improve catalytic performance.[42]

3.3. X-ray photoelectron spectroscopy (XPS)

X-ray photoelectron spectroscopy (XPS) was carried out in order to investigate the electrical states, valences, and chemical compositions of the constituent elements present in the samples. than 1 eV.

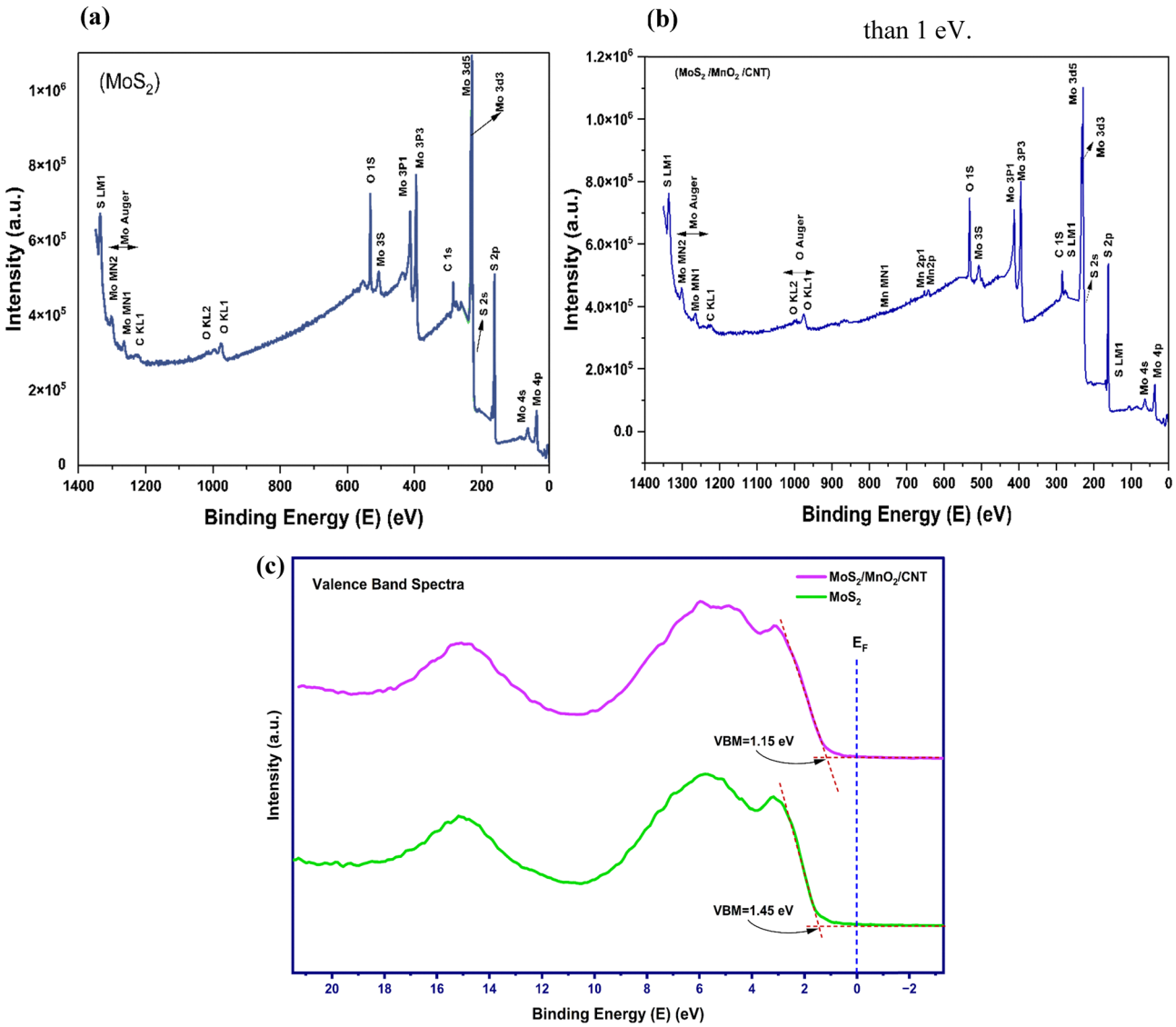

Fig. 5 (a) and (b) Survey spectra and (c) valence band spectra of XPS analysis of the MoS_2 nanoflower and MoS_2/MnO_2 (5 wt%)/CNT (1 wt%) composites, respectively.

This analysis was based on the binding energies that are related to each element. Al K alpha was used as a source of X-rays. When comparing the XPS survey spectra of the pure MoS_2 NFs (Fig. 5a) and the MoS_2/MnO_2/CNT composite (Fig. 5b), Mo 3d and S 2p peaks are clearly observed in both, but the composite additionally shows distinct Mn 2p and enhanced O 1s signals from MnO_2, as well as a sharper C 1s peak from CNTs. In the case of pure MoS_2 NFs the Auger peaks for Mo, which are Mo MN1 and Mo MN2 are observed in the energy range of 1254–1310 eV. The O 1s peak and Auger peaks O KL1 and O KL2 (965–1010 eV) are also observed. The edges and defect sites of MoS_2 are prone to oxidation under ambient circumstances. This results in the formation of Mo–O bonds or oxysulfide species. The O 1s peak is also observed when airborne water, hydroxyls or organic residues absorb onto the surface. These factors contribute to the O 1s signal within the range of 529–531 eV. A shoulder is also observed in the Mo 3d region (235–236 eV), which denotes that Mo is oxidized to Mo^{6+}.[43] The X-ray photoelectron spectroscopy (XPS) valence band spectra (Fig. 5c) analysis of the synthesized MoS_2 NF and ternary composite MoS_2/MnO_2/CNT composite was conducted to analyze the electronic structure and charge transfer pathways. Valence band spectra analysis revealed that the valence band maximum (VBM), determined by linear extrapolation of the leading edge to the baseline, was located at around 1.45 eV for the MoS_2 nanoflower and around 1.15 eV for the MoS_2/MnO_2 (5 wt%)/CNT (1 wt%) composite.[44] The ternary composite VBM is therefore around 0.30 eV closer to the Fermi level (EF). The observed 0.30 eV VBM shift toward EF in the composite is consistent with previously reported VBM shifts of 0.1–0.4 eV in MoS_2 based heterostructures.[45] Valence band spectra indicate a consistent electron transfer mechanism in the ternary composite. At equilibrium, electrons move from MoS_2 into the MnO_2 and CNTs. This produces interfacial band bending.[39] These changes are consistent with providing conductive states of CNTs and MnO_2 accepting electrons *via* reduction or defect states. Together, these observations explain the improved electronic conductivity, charge-storage behavior, and supercapacitive properties of the composite.[21,45] The electron transfer behavior of the ternary composite can be understood as three linked pathways that operate during electrochemical measurements. First, through direct transfer at the MoS_2/MnO_2 interface where Mo 4d and S 3p states couple to Mn 3d orbitals, allowing MoS_2 to donate electrons to MnO_2. This enables partial Mn^{4+} to Mn^{3+} reduction that uses pseudocapacitive sites of MnO_2. Secondly, through the MoS_2/CNT/MnO_2 interface where CNTs act as a highly conductive backbone that accepts charge from MoS_2 and rapidly transmits electrons laterally to MnO_2 or the current collector, thereby lowering charge-transfer resistance and improving rate capability.[44] Finally, through the method of bidirectional coupling during charge–discharge when the potential reverses. In this case, CNTs shuttle electrons back and MnO_2 can return electrons to MoS_2/CNT, so the composite supports fast and reversible exchange between CNT/MoS_2 and redox reservoirs like Mn.[25] Importantly, the valence spectra findings also agree with the electrochemical results, such as the composite exhibiting a lower charge transfer resistance (R_{ct}) in EIS (Fig. 7), faster charge–discharge kinetics in GCD (Fig. 10), and a larger pseudocapacitive contribution in CV (Fig. 9). Together, the spectroscopic and electrochemical signatures give a simple, consistent outcome where CNTs provide fast electronic highways, MnO_2 provides redox sites that accept electrons from MoS_2, and MoS_2 functions as the initial electron donor. Thus this synergistic coupling explains the improved conductivity and charge-storage performance of the ternary composite. A narrow scan spectrum is obtained within a limited binding-energy range in Fig. 6. Peak resolution has been enhanced to achieve a full width at half maximum of less than 1 eV.

Subtle chemical variations, spin orbit components, oxidation states, and bonding conditions are distinctly recognized.[46] These elements are not apparent in survey scans. In the case of the composite, the Mo 3d doublet from MoS_2 (Mo^{4+}) appears with $3d_{5/2}$ at 228.8 eV and $3d_{3/2}$ at 232.5 eV. From Fig. 6(a), it is observed that the energy difference between this doublet is around 3.2 eV, which is consistent with the standard spectrum of MoS_2. These binding energies correspond to Mo^{4+} in MoS_2. As some amount of edge Mo are oxidized to MoO_3 (Mo^{6+}), additional peaks appear at higher BE around 232.2 eV for $3d_{3/2}$ and 236.38 eV for $3d_{5/2}$. Mo is bound to S in the dichalcogenide lattice. Due to interfacial interactions, the peak such as Mo $3d_{5/2}$ (Mo^{6+}) has slightly shifted ($\pm$0.2 eV) from its standard positions.[47] Due to partially oxidized Mo, where MoS_2 is exposed to moisture or air, an intermediate Mo^{5+} state (Mo–OH) is detected with 228.48 eV. This corresponds to incomplete oxidation or hydroxylation confirmed by an O 1s peak at 531.5–532 eV indicating a surface OH group.[48] These characteristic peaks denote the presence of Mo^{4+} in the composite. In the S 2p region shown in Fig. 6(b), we observe the S^{2-} doublet of MoS_2 at 162.3 eV for $2p_{3/2}$ and 163.4 eV for $2p_{1/2}$. These peaks are characteristic of sulfide ions in MoS_2. This doublet is the fingerprint of S^{2-} in a 2H-MoS_2 lattice, as most of the sulfur comes from MoS_2 nanoflowers. For this reason, S^{2-} has an extremely high intensity. Strong S^{2-} peaks confirm MoS_2 formation.[49] The S $2p_{3/2}$ peak is slightly shifted to 162.5 eV and the $2p_{1/2}$ peak to 164 eV. This shift is caused by sulfur atoms located at MoS_2 edges or defect sites. These S atoms experience a different local chemical environment compared to the bulk 2H phase. Hydrothermal growth often produces under-coordinated edge sulfur atoms. These edge or dangling S atoms have slightly lower electron density. This decreases screening and causes their binding energies to shift higher by around 0.8–1 eV.[50] There are some other peaks that appear at higher binding energies near 169 eV for S $2p_{3/2}$ and 170.5 eV for S $2p_{1/2}$. These peaks come from S–O bonds, such as SO_4^{2-} or SO_3^{2-}. Even well-synthesized MoS_2 can develop a thin oxidized or hydroxylated layer when it is exposed to air or water during hydrothermal synthesis. These species are usually only a small fraction of the total sulfur.[51] In the Mn 2p spectrum in Fig. 6(e), there is a doublet with $Mn2p_{3/2}$ at 642.2 eV and $2p_{1/2}$ at 653.9 eV. Additionally, there is a spin–orbit splitting of around 11.7 eV, which is consistent with the standard Mn^{4+} spectrum for MnO_2. Deconvolution also reveals components at lower BE (641 eV), indicating the existence of Mn^{2+}.[52]

A notable feature of Mn is the presence of a weak satellite peak at about 647 eV, which is higher than the main $2p_{3/2}$ peak

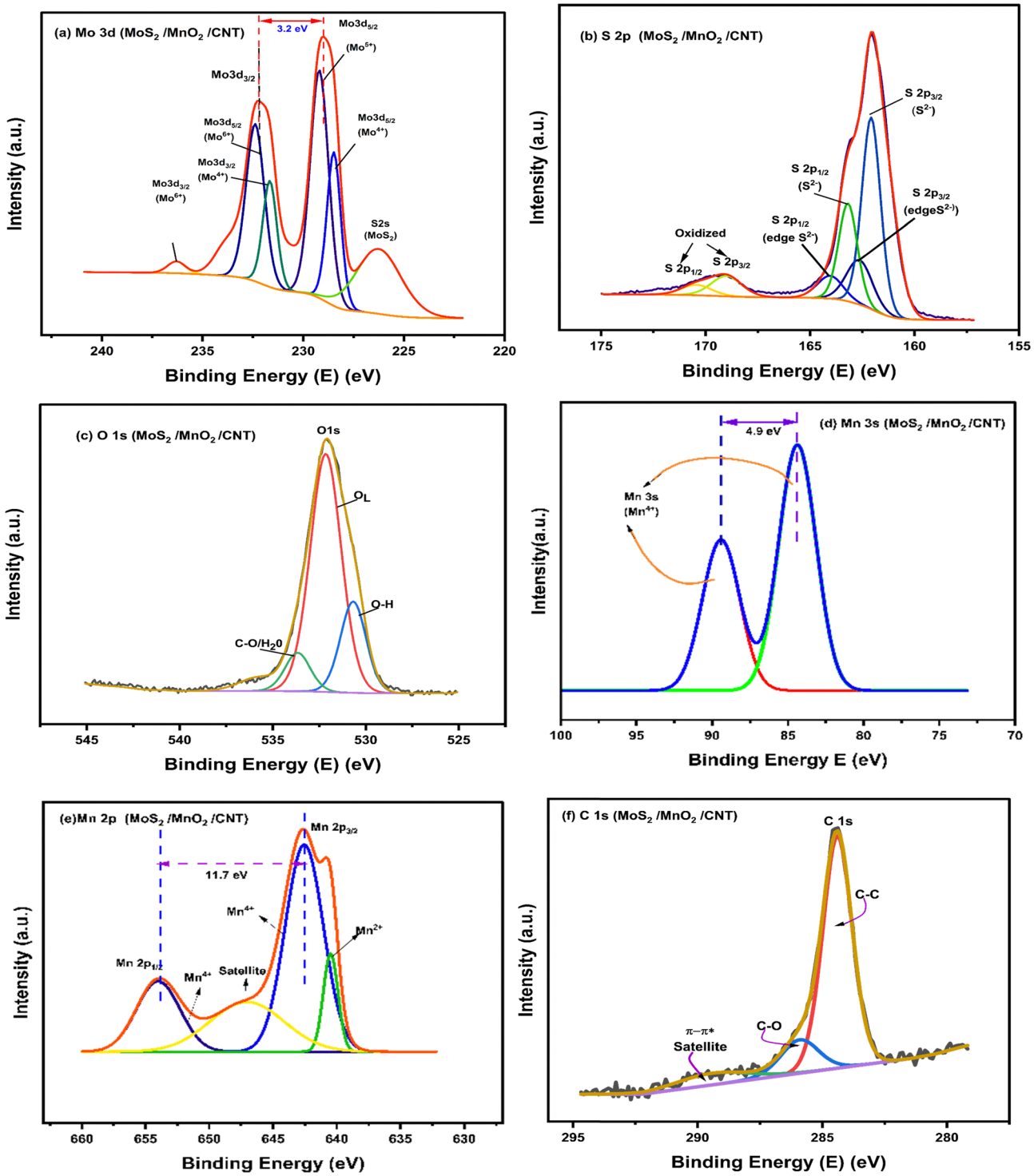

Fig. 6 Narrow spectra of XPS analysis of the MoS_2 nanoflowers and MoS_2/MnO_2 (5 wt%)/CNT (1 wt%) composites, respectively; (a)–(f) represents the narrow spectra of Mo 3d, S 2p, O 1s, Mn 3s, Mn 2p, and C 1s, respectively.

by ~5 eV. For the MnO_2 (Mn^{4+}) spectrum, the MnO satellite appears near 646–647 eV.[53] Thus, the presence of a weak satellite at 647 eV confirms the existence of Mn^{2+}. The synthesis of Mn^{4+} is also confirmed by the absence of a strong satellite peak. The Mn 3s peak in Fig. 6(d) splits into two components due to exchange interactions between the core hole and unpaired 3d electrons.[54] The energy difference ΔE between the two peaks decreases as the oxidation state of Mn increases. From Fig. 6(d) it is observed that the energy difference between the two peaks is around 4.9 eV, which confirms the presence of Mn^{4+} in the MnO_2 nanorod.[55]

In the O 1s spectrum in Fig. 6(c), a strong peak at a binding energy of 532 eV is observed that corresponds to lattice O^{2-} as

Mn–O bonds in MnO_2 and to some extent, Mo–O. A component near 530.5 eV arises from Mn–OH or Mo–O–H. There is also an another higher BE shoulder at 533.8 eV from physisorbed H_2O or C–O from carbonates or organic contamination.[47] Additionally, the FTIR technique was employed to verify the presence of water in Fig. S4. These broad O–H signals are common in MoS_2 and MnO_2 because of the presence of water or hydroxyl groups on their surfaces.[56]

Since only 1 wt% CNT is present, the C signal is weak relative to the survey spectra but still visible in narrow spectra in Fig. 6(f). The C 1s region is dominated by sp^2 carbon from CNT. The C–C bond corresponds to the main peak at 284.6 eV. This will overlap with adventitious carbon contamination.[57] Weaker features at 286 eV are due to the existence of C–O (C–OH/C–O–C).[58] A π–π^* shake-up satellite around 6 eV above at 290 eV, the main C–C peak is also observed. Extended delocalized electrons in a sample can produce satellite structures, which are several eV above the binding energy of the primary peak.[59]

3.4. Electrochemical impedance spectroscopy (EIS)

Electrochemical impedance spectroscopy was carried out in the frequency range 1 Hz to 10^6 Hz to understand the charge transfer resistance and the kinetic feature of the ion diffusion responsible for the charge storage property of the electrode.[60] Fig. 7 illustrates the Nyquist plots of the MoS_2, MoS_2/MnO_2 (3 wt%, 5 wt%) and MoS_2/MnO_2 (5 wt%)/CNT (1 wt%). The lower inset of Fig. 7(a) demonstrates an enlarged view of the high frequency region of the Nyquist plots. The Nyquist plot for the pure MnO_2 nanorods is shown in Fig. S6(b). The solution resistance (R_S) of the electrochemical systems is represented by the real axis intercept of the Nyquist curve at the high frequency region. This indicates the equivalent series resistance, which is made up of the bulk resistance such as the ionic resistance of the electrolyte and the contact resistance between the active material and the current collector.[61]

The interfacial charge transfer resistance (R_{ct}) between the active material and electrolyte is given by the diameter of the semicircle. The slanted line in the low-frequency region of the Nyquist plots corresponds to the mass transfer resistance (Warburg impedance, Z_W) governed by a diffusion process.[62] In Fig. 7(a and b), the synthesized ternary composite starts at a small but non-zero intercept on the x-axis, indicating the solution resistance, R_S. The diameter of the semicircle in the Nyquist plots in Fig. 7(b), significantly decreases from MoS_2, MoS_2 with 3 wt%, 5 wt% MnO_2 to 5 wt% MnO_2/1 wt% CNT, indicating a significant decrease in charge transfer resistance (R_{ct}). Due to the large interlayer distance of the MoS_2/MnO_2 (5 wt%)/CNT (1 wt%) nanocomposite, the electrolyte gets easy access, and as a result, charge transfer resistance decreases. Again, the steeper slope of the MoS_2/MnO_2 (5 wt%)/CNT (1 wt%) line as compared to MoS_2 and other two binary composites yields a lower Z_W. This indicates the faster diffusion capability of electrons and electrolyte ions on its surface.[60]

The electrochemical impedance spectra of the synthesized samples were then successfully fitted using an equivalent circuit model incorporating a constant phase element (CPE) with diffusion, as illustrated in the inset of Fig. 7(b), providing a reliable representation of the charge transfer and ion diffusion processes in the electrodes. Here, in the equivalent circuit W, R_S, R_{ct}, and CPE denote the Warburg impedance, solution resistance, charge transfer resistance and constant phase element, respectively. Constant phase element (CPE) is used instead of a regular capacitor because it can account for inconsistencies in the material, like the uneven structure and imperfections on the microscopic level, specifically, the rough and porous surface of the electrode. This kind of surface is responsible for double-layer capacitance.[63]

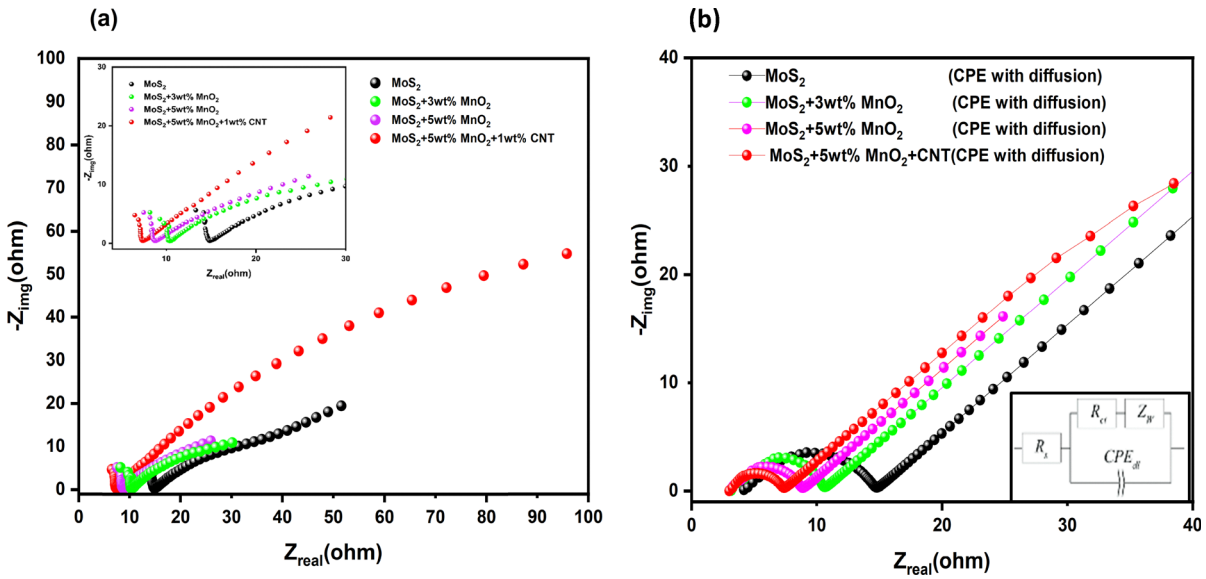

Fig. 7 (a) Nyquist plot of the synthesized MoS_2 nanoflower, MoS_2/MnO_2 (3 wt%), MoS_2/MnO_2 (5 wt%) and MoS_2/MnO_2 (5 wt%)/CNT (1 wt%) nanocomposites, respectively; (b) CPE with diffusion fit with the equivalent circuit.

Table 2 The equivalent circuit values for EIS fitting

Sample	R_s (Ω)	R_{ct} (Ω)	Warburg (Ω)
MoS_2	5.71	10.55	23.82
MoS_2/MnO_2 (3 wt%)	5.67	7.313	15.68
MoS_2/MnO_2 (5 wt%)	5.56	5.755	17.53
MoS_2/MnO_2 (5 wt%)/CNT (1 wt%)	5.33	4.262	10.09

Table 2 represents the charge transfer kinetics parameters of the electrodes denoting the resistances, constant phase element and Warburg element values as obtained by fitting the Nyquist data to the equivalent electrical circuit model shown in the lower inset of Fig. 7(b). As seen from the data in Table 2, modifying MoS_2 with MnO_2 and adding CNTs significantly enhances its electrochemical characteristics. Pure MoS_2 exhibits the highest charge transfer resistance (10.55 Ω) and Warburg impedance (23.82 Ω), indicating the lowest efficiency in electron and ion transport. As the proportion of MnO_2 increases to 5 wt%, both resistances decrease, with R_{ct} (charge transfer) dropping to 5.755 Ω and Warburg to 17.53 Ω, suggesting improved electrical conductivity, high wettability, higher rate capability, increased reaction rates of the electrode, and better efficiency.[64,65] The introduction of 1 wt% CNT to the MoS_2/MnO_2 (5 wt%) composite further reduces both R_S (5.33 Ω) and R_{ct} (4.262 Ω) to their lowest values while simultaneously minimizing Warburg impedance (10.09 Ω), which reflects superior charge storage capacity and faster ion diffusion. The increasing interlayer distance facilitates electrolyte access to the active material, hence reducing charge transfer resistance as the concentration of MnO_2 and CNT in the MoS_2 nanoflower is increased.[66] The quantitative analysis shows that the ternary composite has the lowest charge transfer resistance and improved ion diffusion. Thus, it is the best performer electrochemically among the samples. In Fig. 8(a and b) after 2000 cycles of charging and discharging, the Nyquist plots of the synthesized nanocomposite showed a smaller semicircle diameter indicating the decrease in charge transfer resistance. Because after continuous charge and discharge cycles, the intertwined CNT web in the MoS_2/MnO_2/CNT composite has settled into even better electrical contact, while the MoS_2 layers have gently peeled apart to reveal more active edge sites and the MnO_2 has developed tiny fissures that let the electrolyte in more easily. Together, these changes mean the electrolyte wets the electrode more thoroughly, electrons find smoother pathways through the CNT network so overall it takes less effort for charge to move across the interface, and that results in a smaller semicircle in the Nyquist plot.[67]

3.5. Cyclic voltammetry (CV)

The cyclic voltammogram of MoS_2, MoS_2/MnO_2 (3 wt%, 5 wt%) and MoS_2/MnO_2 (5 wt%)/CNT (1 wt%) were obtained within a potential window of −0.4 V to +0.4 V at various scan rates ranging from 10 mV ps to 80 mV ps as shown in Fig. 9(a–e). In Fig. 9(a), pristine MoS_2 shows the lowest current response, which is 0.5×10^2 mA g^{-1} at a scan rate of 10 mV ps, resulting in the smallest enclosed CV area. The highest current response is found at 80 mV ps which is 1.4×10^2 mA g^{-1} for voltage 0.4 V and -1.4×10^2 mA g^{-1} for a reversible voltage −0.4 V. The leaf like quasi rectangular shape confirmed mixed EDLC and pseudocapacitive nature but overall limited performance.[68] From Fig. 9(b and c), as 3 wt% and 5 wt% MnO_2 nanorods are added, the current response increases to 3.3×10^2 mA g^{-1} at voltage 0.4 V at a scan rate of 80 mV ps and the CV area was seen to be larger than that of pristine MoS_2. The curve being slightly deviated from the rectangular shape indicates the contribution of the intended pseudocapacitance from MnO_2.[69] Finally, addition of 1% CNT to the binary 5 wt% MnO_2 incorporated MoS_2 nanoflower exhibits a significantly larger current response, which is almost 7 times larger than the other samples. The current response jumped to 20×10^2 mA g^{-1}. Fig. S6(a)

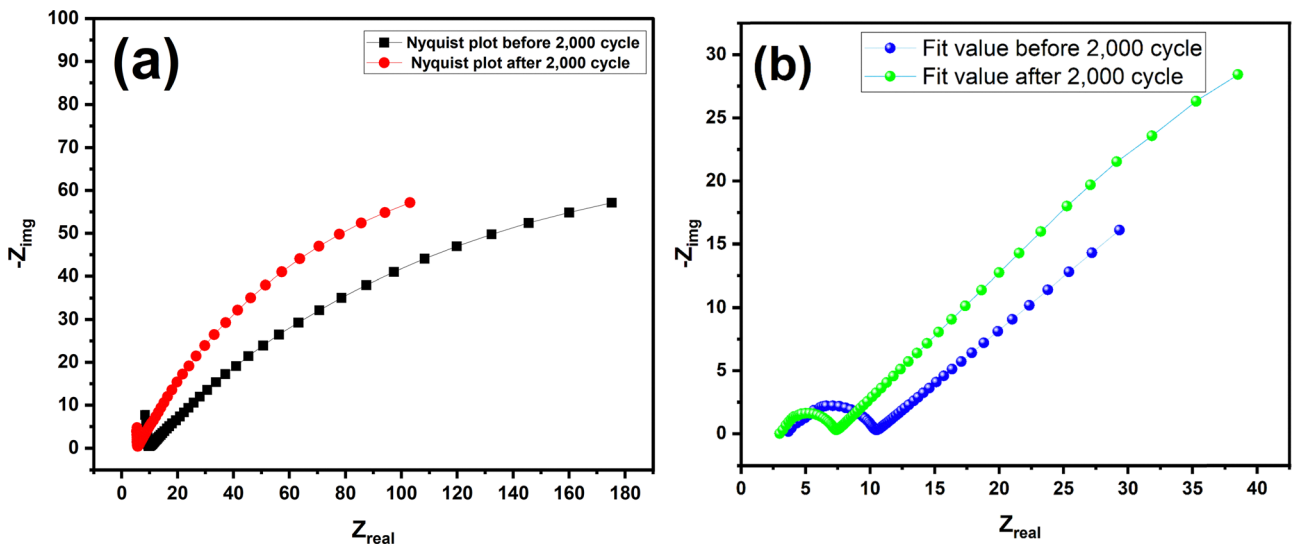

Fig. 8 Nyquist plots of the MoS_2/MnO_2 (5 wt%)/CNT (1 wt%) nanocomposite (a) before and after 2000 cycles of charging–discharging and (b) fitted before and after 2000 cycles of charging–discharging.

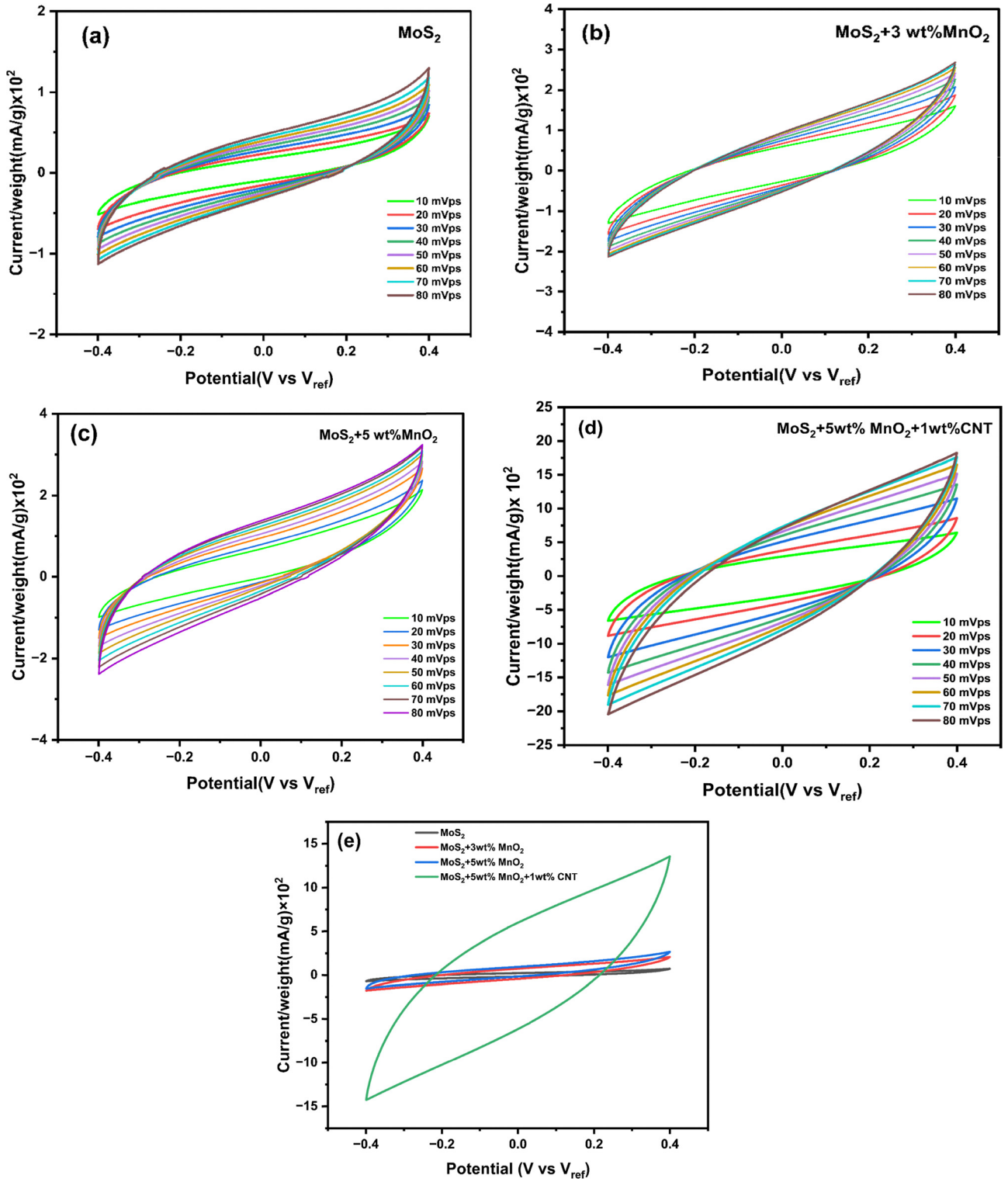

Fig. 9 CV plots at different scan rates of (a) MoS_2, (b) MoS_2/MnO_2 (3 wt%), (c) MoS_2/MnO_2 (5 wt%) (d) MoS_2/MnO_2 (5 wt%)/CNT (1 wt%), and (e) CV plot for all samples at a scan rate of 30 mV ps.

represents the CV plot for the pure MnO_2 nanorod. The vastly increased area of the CV loop points to a massive enhancement in the specific capacitance. The shape remains mostly symmetrical even as the scan rate is increased to 80 mV s^{-1}, indicating excellent high-rate capability. The addition of CNTs acts as the critical enabler, creating a highly conductive network.[70]

Thus, the final composite exhibits synergistic effects, including the high capacitance of MoS_2 and MnO_2 and excellent

conductivity of CNTs, resulting in a hierarchical electrode with significantly higher specific capacitance and superior rate capability than any of its sub-components. For all materials, a clear and consistent trend is observed where the peak currents (or the overall current response at any given potential) increase proportionally with increasing scan rate (Fig. 9a–d). This is a fundamental characteristic of electrochemical processes, where faster potential sweeps necessitate higher rates of electron transfer and ion movement to maintain the electrochemical reaction. To assess the relative capacitive performance, a comparative CV plot in Fig. 9(e) directly compares the CV profiles of the MoS_2, MoS_2/MnO_2 (3 wt%, 5 wt%) and MoS_2/MnO_2 (5 wt%)/CNT (1 wt%) materials at a constant scan rate of 30 mV ps. The more rectangular shape and larger area of the CV curves from the original material to the binary composite indicate a steady improvement in capacitive performance. The K^+ cation has a great impact on the charge–discharge electrochemistry of the MoS_2 NF and MoS_2/MnO_2/CNT nanocomposites (Fig. 12). The surface reaction and intercalation mechanism are as follows:

$$MoS_2 + K^+ + e^- \leftrightarrow (MoS_2\text{-}K^+)(\text{surface}) \quad (6)$$

$$MnO_2 + K^+ + e^- \leftrightarrow (MoS_2\text{-}K^+)(\text{surface}) \quad (7)$$

$$CNT + K^+ + e^- \leftrightarrow (CNT\text{-}K^+)(\text{surface}) \quad (8)$$

$$(MoS_2/MnO_2)_{\text{surface}} + K^+ + e^- \leftrightarrow ((MoS_2/MnO_2) - K^+)(\text{surface}) \quad (9)$$

$$(MoS_2/MnO_2/CNT)_{\text{surface}} + K^+ + e^- \leftrightarrow ((MoS_2/MnO_2/CNT) - K^+)(\text{surface}) \quad (10)$$

$$MoS_2 + K^+ + e^- \leftrightarrow MoS - SK(\text{intercalation}) \quad (11)$$

$$MnO_2 + K^+ + e^- \leftrightarrow (MnO - OK)(\text{intercalation}) \quad (12)$$

$$MoS_2/MnO_2 + K^+ + e^- \leftrightarrow (MoS_2/MnO_2)K(\text{intercalation}) \quad (13)$$

$$MoS_2/MnO_2/CNT + K^+ + e^- \leftrightarrow (MoS_2/MnO_2/CNT)K(\text{intercalation}) \quad (14)$$

The ternary composite exhibits a dramatic and overwhelming increase in current response, resulting in a significantly larger enclosed area compared to all other material systems (Fig. 9e). The overall current density is orders of magnitude higher than that of pure MoS_2. The profound leap in electrochemical performance upon CNT addition, particularly when combined with MnO_2, signifies a synergistic effect rather than a mere additive contribution.[71] Addition of 1 wt% CNT shows a dramatic increase in current response and CV area, providing efficient electron transport pathways, reducing internal resistance and ensuring better utilization of active materials.[72] As a layered transition metal dichalcogenide, MoS_2 possesses a unique structure that can facilitate the intercalation of ions.[73] This lowers resistance and boosts overall charge transfer. This improved conductivity helps ions move faster and reach active sites more easily, which explains the sharper peaks and higher currents even at high scan rates. The ''leaf-like'' shape clearly shows better charge transfer. Overall, this composite stands out as the most efficient performer for fast, high-capacity energy storage.[74]

3.6. Galvanostatic charge discharge

Galvanostatic charge discharge was performed to assess how well the supercapacitor works and how long its cycle life is. To verify the supercapacitive performance of the synthesized MoS_2/MnO_2/CNT nanocomposite materials, GCD tests were conducted at various current densities within a voltage window of −0.40 V to 0.40 V in Fig. 10(a–d). All the curves exhibit nonlinear characteristics and mild distortion during both charging and discharging. This indicates the involvement of pseudocapacitance due to redox processes. This trend also aligns with the CV results (Fig. 9). The discharge duration of the composites exceeds that of pure MoS_2 NF base. This means that the incorporation of MnO_2 nanorods and CNTs has significantly enhanced the capacitive performance. There is a drop in voltage at the start of the discharge process in GCD testing, which is known as the *iR* drop. Internal resistance in the electrode material causes this drop, leading to the loss of energy in the form of heat.[75] The MoS_2/MnO_2 (5 wt%)/CNT (1 wt%) composite had the smallest *iR* drop in our experiments compared to the other samples.

This signifies that it has lower internal resistance and higher electrical conductivity. Supercapacitors need to have low internal resistance. This helps prevent energy loss during charging and discharging. This leads to better energy efficiency and makes the device more power saving.[76]

Thereby, among all the composites evaluated, the MoS_2/MnO_2 (5 wt%)/CNT (1 wt%) is the most suitable for high-performance, energy-efficient supercapacitors. To determine the specific capacitance (C_s), the required formula is:

$$C_s = \frac{i \times \Delta t}{m \Delta V} \quad (3)$$

In this context, i represents the discharge current, Δt denotes the discharge duration, m indicates the mass of the active material, and ΔV refers to the potential window width. From Fig. 11(a), it can be observed that the specific capacitance for MoS_2 NF, MoS_2 NF/MnO_2 nanorod (3 wt%), MoS_2 NF/MnO_2 nanorod (5 wt%), and MoS_2 NF/MnO_2 nanorod (5 wt%)/CNT (1 wt%) at the 0.15 A g^{-1} current density was 14 F g^{-1}, 68 F g^{-1}, 120 F g^{-1}, and 457 F g^{-1}, respectively.

The MoS_2 NF/MnO_2 (5 wt%)/CNT (1 wt%) nanocomposite outperforms the other samples in terms of discharge time and specific capacitance. In the GCD curves in Fig. 10(a–d), the discharge duration of the material likewise improves when the concentration of MnO_2 nanorods in the nanocomposite increases, and that is highest when 1 wt% CNT was added to the nanocomposite. This indicates that the capacitive behavior of MoS_2 NF has enhanced. In Fig. 10(e), the charge–discharge curve was shown under the specific current density of 0.15 A g^{-1}. The ternary composite exhibits the largest discharging time among all the samples.

All the nanocomposites with embedded electrode MoS_2 NF, MoS_2 NF/MnO_2 nanorod (3 wt%), MoS_2 NF/MnO_2 nanorod

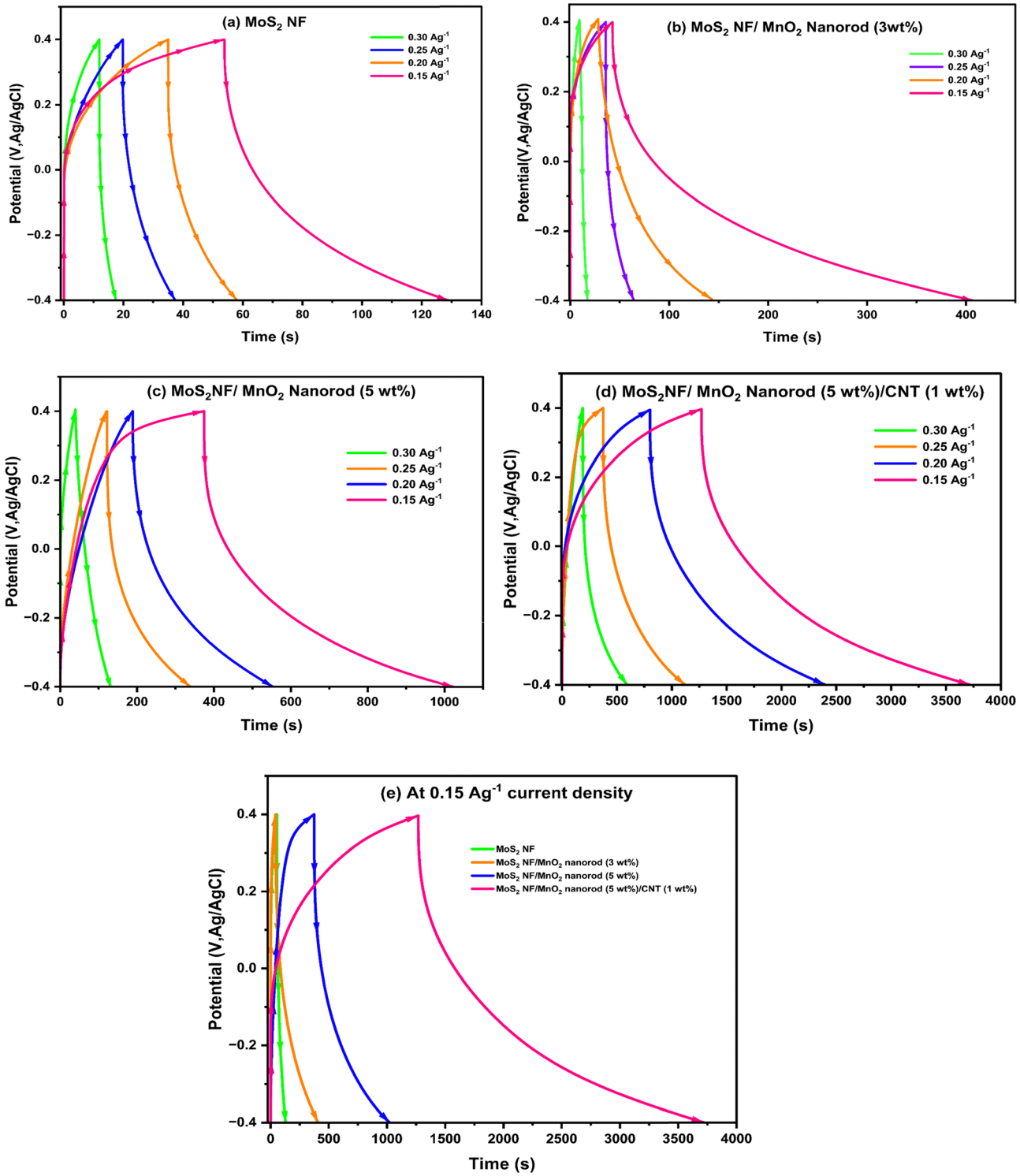

Fig. 10 (a)–(d) Galvanostatic charging–discharging curves of the MoS_2 nanoflower, MoS_2/MnO_2 (3 wt%), MoS_2/MnO_2 (5 wt%) and MoS_2/MnO_2 (5 wt%)/CNT (1 wt%) nanocomposites; (e) represents galvanostatic charging–discharging curves of the nanocomposites at 0.15 A g^{-1}.

(5 wt%), and MoS_2 NF/MnO_2 nanorod (5 wt%)/CNT (1 wt%) display distinctive pseudocapacitive behavior, which is further verified by the voltage plateaus observed in the discharge curves.[77,78]

The charging and discharging durations are reduced with an increase in current density. This occurs because the electrolyte ions do not have sufficient time to get to all of the electrode's active sites for a complete reaction. Thus, when the current density increases, the specific capacitance decreases. The redox processes slow down with larger currents because the electrolyte and electrode do not have as much time to come into contact. Ions are unable to penetrate further into the electrode and instead interact with its outer surface. Whereas ions are more

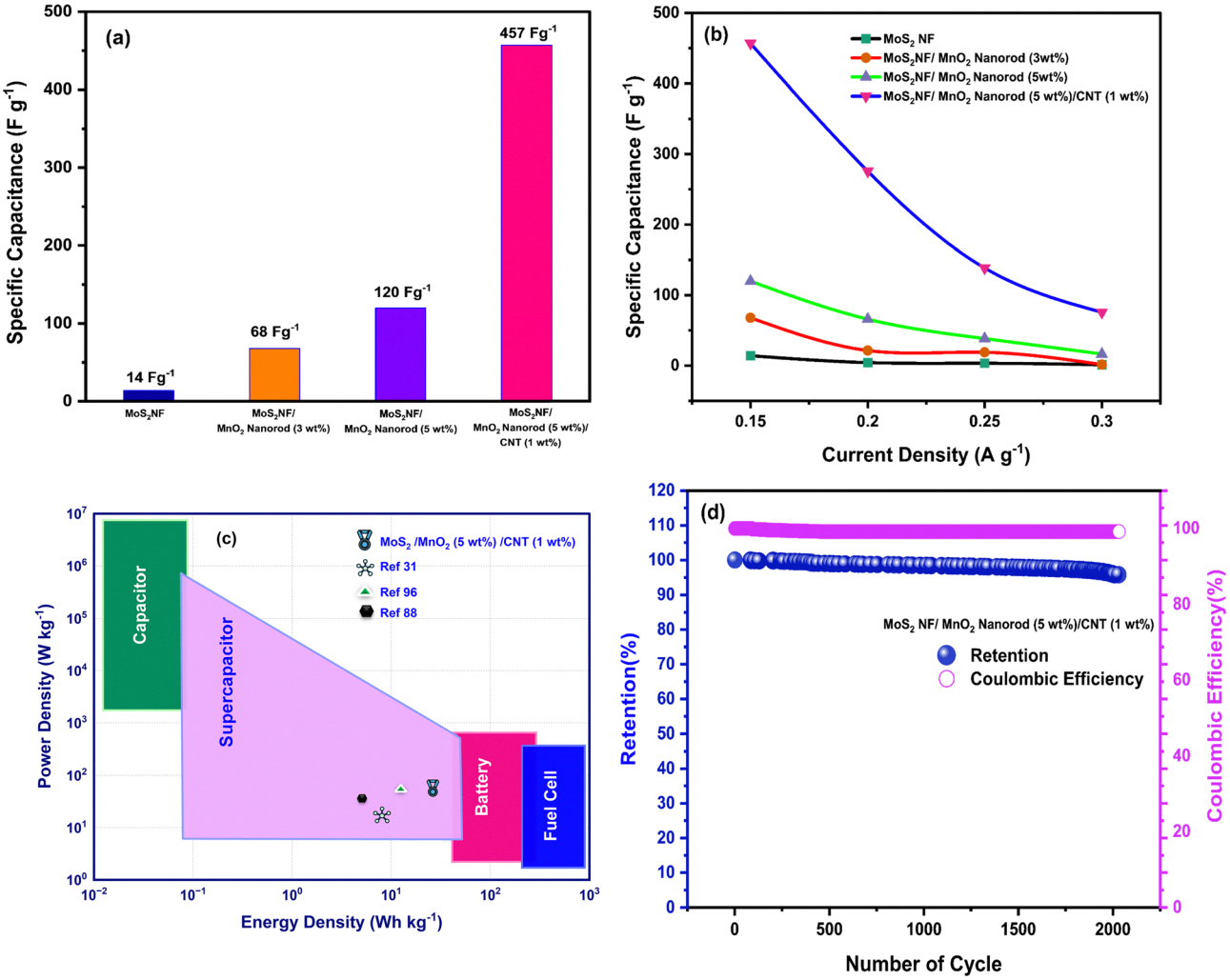

Fig. 11 (a) Comparison of the specific capacitances for each sample at 0.15 A g^{-1}; (b) variation of specific capacitance with increasing current densities; (c) Ragone plot (power density *vs.* energy density) for the synthesized samples; (d) capacitance retention and coulombic efficiency of the MoS_2/MnO_2 (5 wt%)/CNT (1 wt%) nanocomposite over 2000 cycle of charging–discharging.

easily able to penetrate the interior pores of the electrode and react with more active sites with lower current densities. This results in greater specific capacitance (C_s). In Fig. 11(b), the specific capacitance varies with increasing current density for all the samples, as shown in a graph. We analyzed the effect of current density on the specific capacitance (C_s) of the electrodes. From the plot (Fig. 11b) it can be observed that at the current density of 0.15 A g^{-1} the specific capacitance was the highest for the ternary composite. Because of superior ion transport and conductivity, the MoS_2/5% MnO_2/1% CNT material retains a higher C_s even at high currents as well. In the design of a practical energy storage system, power density (P) and energy density (E) are quite important. The GCD curves of the synthesized samples were used to determine energy density (Wh kg^{-1}) and power density (W kg^{-1}) according to eqn (16) and eqn (17):

$$E\left(\mathrm{Wh\,kg^{-1}}\right) = \frac{C_s \times V^2}{2 \times 3.6} \tag{15}$$

where C_s is the specific capacitance and V is the working potential window.

$$P\left(\mathrm{W\,kg^{-1}}\right) = \frac{E}{\Delta t} \times 3600 \tag{16}$$

where E is the energy density and Δt is the discharging time.

Fig. 11(c) represents the Ragone plot. The vertical axis represents energy density, while the horizontal axis represents power density. At a current density of 0.15 A g^{-1}, the energy and power densities of the nanocomposites were measured. The MoS_2 NF/MnO_2 nanorod (5 wt%)/CNT (1 wt%) composite provided the highest energy density of 37 Wh kg^{-1}, at a power density of 60 W kg^{-1}. It achieved enhanced performance due to the synergistic effect of the additives, which improve electron transport and provided more surface area with additional redox sites.[79,80]

The GCD plot for the pure MnO_2 nanorods is shown in Fig. S6(c). As observed, increasing the MnO_2 content raised the capacitance (5 wt% > 3 wt% MnO_2). The MoS_2/MnO_2 (5 wt%) electrode likely had more redox sites than 3% MnO_2, so its

specific capacitance was higher. However, while 5% MnO_2 alone can raise the composite's resistance, the addition of CNT in this case mitigated that effect. In fact, adding just 1% CNT to MoS_2/MnO_2 (5 wt%) showed a much larger boost (457 F g^{-1}) than MoS_2/MnO_2 (5 wt%) without CNT.[81] This is because the CNT network made most MnO_2 and MoS_2 capacitance sites accessible. Also, in EIS (Fig. 7), it shows that the CNT containing sample has a significantly smaller semicircle (lower R_{ct}) and more vertical low-frequency line, reflecting faster ion diffusion and charge transfer. Similarly, the CV curves in Fig. 9 would likely become enlarged in area when CNT is added, showing combined double-layer and redox behavior.[82]

3.7. Electrode stability analysis

Cycling stability was performed on the nanocomposite embedded electrode to inspect the capacity to maintain particular capacitance during successive charge–discharge cycles. At a current density of 0.15 A g^{-1}, 2000 charging–discharging cycles were performed for the MoS_2/MnO_2/CNT ternary composite. It is evident from Fig. 11(d) that retention of the ternary composite dropped to around 96% after 2000 cycles. This indicates the increasing capacity for retention and durability as well. The coulombic efficiency remains 100%, which indicates that there are no side reactions consuming charge, such as electrolyte decomposition, parasitic reactions or self-discharge.[83]

In MoS_2 NF, the nanosheets stick together by weak van der Waals forces, and ions intercalate between the layers and make them expand during each charge–discharge cycle. This introduces strain on the sheets and finally breaks them. The sheets eventually fall back down and stick together, covering up active surfaces and closing pores.[84] The layers peel off one by one in certain locations, leaving behind microscopic pieces that make the framework weaker. When the volume varies a lot, the whole electrode material falls apart and loses touch with the current collector. Edge or point flaws and conversion reactions also break down the original layered shape. As the material breaks down, its ability to conduct electricity goes down, its impedance to charge transfer goes up, and its ion routes get obstructed. Slow ion mobility and particle separation lead to the capacitance declining fast in the end. MoS_2 is intrinsically a poor electrical conductor, so its performance is limited by electron transport that worsens more with cycling due to structural changes.[85] For this reason, the MoS_2 NF exhibits poor cycling stability. The ternary composite combines 3D MoS_2 nanoflowers, 5 wt% MnO_2 nanorods and 1 wt% CNTs to achieve synergistic enhancements in capacitance and cycling stability. The interplanar spacing of the MoS_2 nanoflowers is increased by the incorporation of MnO_2 nanorods and CNTs. This results in a defect-rich structure and structural modification that creates additional reactive sites and improves charge collection capacity.[16] The size of the crystallites goes down while the microstrain and dislocation density increase. These changes create additional edge sites and worsen surface defects. The increase in lattice strain and dislocations (Fig. 3) makes it easier for ions to move around and lets more redox reactions happen. These features work together to improve conductivity, charge transfer, and ion diffusion. On the other hand, the MoS_2 nanoflower network offers a high surface area scaffold for fast ion access, while the MnO_2 nanorods introduce abundant redox active sites.[10] MnO_2 nanorods provide substantial pseudocapacitance through rapid surface redox reactions. The MnO_2 nanorods mechanically stabilize the structure.[86] However, excessive loading can form thick, poorly conductive layers that impede ion transport.[17] It also preserves high ionic conductivity that is essential for performance.

The rod-like morphology of the material acts as a spacer, preventing the restacking of MoS_2 layers, which ensures stable interlayer spacing and enhances charge transfer kinetics.[87] CNTs possess electrical conductivity values of 10^4–10^6 S m^{-1}.[88] The 1% CNT loading creates a three-dimensional conductive network that intensely improves electron transport. CNT incorporation significantly reduces charge transfer resistance in composite electrodes.[89] The improved electrical environment due to CNT addition is also evident in the EIS plot (Fig. 7), and also efficient charging and discharging is observed through the GCD plot (Fig. 10). CNTs possess exceptional mechanical properties. This mechanical reinforcement prevents structural collapse during cyclic charge–discharge. The CNT network ensures synergistic stress distribution across the ternary composite. It also effectively prevents microcrack formation and accommodates volume changes during pseudocapacitive reactions.[90]

Thus, the ternary composite structure enables multiple charge storage mechanisms, which are double-layer capacitance from the high surface area MoS_2 nanoflowers, pseudocapacitance from MnO_2 redox reactions, and enhanced conductivity from the CNT network. These features work together to improve conductivity, charge transfer, and ion diffusion. MoS_2/5 wt% MnO_2/1 wt% CNT, the ternary composite, achieves exceptional performance due to a carefully orchestrated combination of various optimization mechanisms. Thus, the ternary composite has the highest specific capacitance of 457 F g^{-1} at 150 mA g^{-1}. The ternary composition creates flexible architectures that accommodate volume changes during cycling without structural failure. The results show that carefully controlling defects and architecture can greatly improve the electrochemical performance of supercapacitors. Table 3 indicates that the MoS_2/MnO_2/CNT electrode demonstrates superior capacitance and stability compared to previously documented MoS_2-based electrodes. This shows how MnO_2 and CNTs work together to add more redox active sites and ensure that there is a conductive network. The combination efficiently suppresses structural degradation while keeping fast charge transport, which makes the composite a good choice for high performance supercapacitor uses.

XRD and SEM were performed on the working electrodes after cycling to identify structural and compositional changes, such as layer delamination, loss of crystallinity or phase dissolution that could directly explain the observed drop in capacitance. XRD and SEM results indicate that delamination of the MoS_2 nanoflowers might be the main cause of the capacity drop. The MoS_2 (002) peak was broadened (Fig. S7) and the nanosheets were witnessed to peel apart, exhibiting

Table 3 Comparison of electrochemical performance and capacitance of MoS_2 based composites with previously reported supercapacitors in the literature

Material of electrode	Electrolyte	Current density (A g^{-1})	Specific capacitance (F g^{-1})	Cycle number	Retained specific capacitance (%)	Ref.
MoS_2 nanosheets	1 M Na_2SO_4	1.0	143.12	5000	87.1	87
MoS_2/reduced graphene oxide (RGO)	1 M KCl	1.0	297	10 000	95.3	91
MoS_2/MnO_2 composite	1 M Na_2SO_4	0.04	193	10 000	94	3
MoS_2 nanosphere	1 M Na_2SO_4	1	518.7	1100	73.5	92
MoS_2-CNT	1 M Na_2SO_4	2	74	1000	80.8	93
MoS_2/MnO_2/CNT	1 M KOH	0.15	457	2000	96	This work

layer separation, and the presence of detached fragments in SEM (Fig. S8). These structural changes disrupt electrical contact and reduce the active surface area. As a result, the material suffers from significant performance decay.[94] The reduction of crystalline MnO_2 reflections shows that some MnO_2 might have dissolved during cycling, which depletes a pseudocapacitive component and thus contributes additionally to the capacity drop. However, this effect is considered minor to the structural degradation of MoS_2 in the ternary composite.[95] Fig. 12 represents the schematic of K^+ and H_2O intercalation/deintercalation in the MoS_2/MnO_2/CNT composite during cyclic charge–discharge in 1 M KOH. During charging, hydrated K^+ enters the MoS_2 interlayers and MnO_2 tunnels (Fig. S5b), inducing slight, reversible expansion and redox activity, while the CNT network (Fig. S5c) ensures rapid electron transport and buffers structural strain. During discharging, K^+ and H_2O are expelled, restoring the original MoS_2 spacing and MnO_2 morphology, with CNTs preserving electrode integrity and conductivity throughout cycling.

4. Conclusions

To sum up, we developed a ternary MoS_2/MnO_2 (5 wt%)/CNT (1 wt%) electrode using a simple hydrothermal method where MoS_2 nanoflowers successfully grew on the MnO_2 nanorods

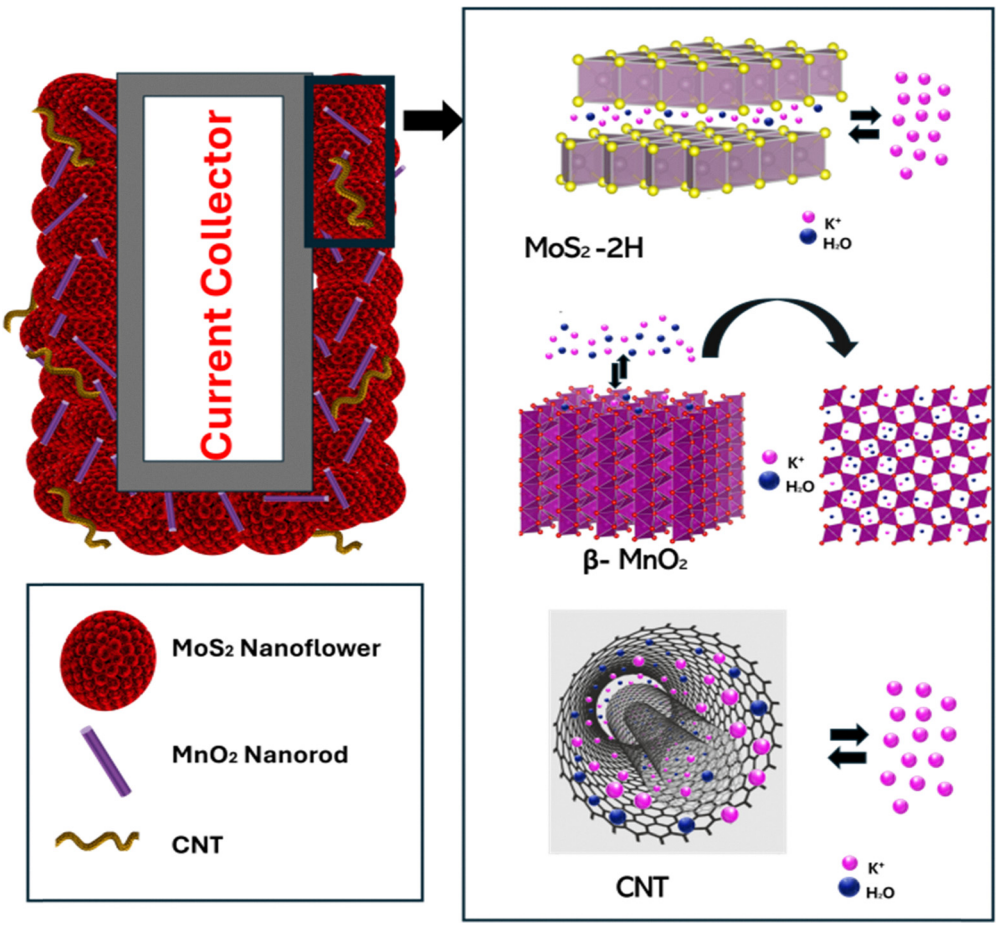

Fig. 12 Schematic of K^+ ion and H_2O insertion and extraction from the electrolyte into the MoS_2/MnO_2/CNT composite electrode.

and CNTs. Through the XRD analysis, it was verified that the phases present in the composite are pure and crystalline in nature. It also confirmed structural integrity and effective incorporation of MoS_2/MnO_2/CNT in the composite with no signs of unwanted phases or impurities. SEM analysis exhibited successful integration among the 3D flower-like morphology and rod and tube-like 1D morphology in the composites with MoS_2 nanoflowers anchored on MnO_2 rods and CNTs connecting them. EIS and CV showed that the charge transfer resistance was small, and the redox kinetics were rapid. XPS and FTIR tests showed that MoS_2/MnO_2/CNTs are all in the proper chemical state and that they are strongly bonded to each other. The best 5 wt% MnO_2 nanorod maximizes the number of pseudocapacitive sites without blocking ion pathways, and the 1 wt% CNT ensures strong electronic conductivity and structural support. In three-electrode configurations among the nanocomposites, the MoS_2/MnO_2 (5 wt%)/CNT (1 wt%) electrode had the highest specific capacitance of 457 F g^{-1} measured at 0.15 A g^{-1}, which is significantly higher than that of the MoS_2 NF base (14 F g^{-1} at 0.15 A g^{-1}). The ternary composite MoS_2/MnO_2 (5 wt%)/CNT (1 wt%) provided an energy density of 37 Wh kg^{-1}, at a power density of 60 W kg^{-1}. After 2000 cycles, cycling stability tests showed that the capacitance retention was 96%, which verifies that the device is very durable. A coulombic efficiency of 100% was attained, which means that the charge stored during charging is fully recovered during discharging, indicating no energy loss due to side reactions. This work shows that precise compositional tuning and hierarchical nanostructuring can make supercapacitor electrodes that store ample energy, enable faster charge–discharge rates, and stay stable for a long time. Because of its exceptional electrochemical performance, enhanced stability and high coulombic efficiency, the MoS_2/MnO_2/CNTMoS_2/MnO_2 (5 wt%)/CNT (1 wt%) ternary nanocomposite electrode material could be an excellent candidate for the development of advanced energy storage systems.

Declaration of generative AI in scientific writing

The authors declare that they did not use AI or AI-assisted technologies in the writing process.

Author contributions

The manuscript was written through the contributions of all authors. All authors have given approval to the final version of the manuscript. Md. Arif Hossain Chowdhury Anik: conceptualization, methodology, investigation, formal analysis, writing – original draft. T. M. A. Iqbal Bin Belal: conceptualization, methodology, investigation, formal analysis, writing – original draft. Md Shafayatul Islam: methodology, formal analysis, writing – review and editing. Koushik Roy Chowdhury: investigation, formal analysis. Mrinmoy Brahma: investigation, formal analysis. Shad Inquiad Mim: investigation, formal analysis. Aninda Nafis Ahmed: methodology, investigation, formal analysis. Ahmed Sharif: conceptualization, resources allocation, supervision, writing – review and editing.

Conflicts of interest

There are no conflicts of interest to declare.

Data availability

The datasets are available upon request from the authors.

The data supporting this article have been included as part of the supplementary information (SI). Supplementary information: Fig. S1: XRD pattern of MnO_2 nanorods. Fig. S2: EDX spectra of the (a) MnO_2 nanorods, (b) MoS_2 nanoflowers, (c) MoS_2/MnO_2 (5 wt%) and (d) MoS_2/MnO_2 (5 wt%)/CNT (1 wt%) nanocomposites, respectively. Fig. S3: (a) SEM images of CNT and (b) MnO_2 nanorods, respectively. Fig. S4: FTIR spectra of the MoS_2/MnO_2 (5 wt%)/CNT (1 wt%) nanocomposite. Fig. S5: Crystal structure of (a) layered 2 H MoS_2, (b) β-MnO_2, and (c) CNTs. Fig. S6: (a) CV, (b) EIS, and (c) GCD plots of MnO_2 nanorods. Fig. S7 XRD pattern of the MoS_2/MnO_2 (5 wt%)/CNT (1 wt%) ternary composite (a) before cycling, and (b) after cycling. Fig. S8 SEM images of the MoS_2/MnO_2 (5 wt%)/CNT (1 wt%) ternary composite (a) before cycling, and (b) after cycling. See DOI: **https://doi.org/10.1039/d5ma00817d**.

Acknowledgements

The authors would like to express their gratitude to the Basic Research Grant of the Bangladesh University of Engineering and Technology (BUET). The authors would also like to express their gratitude to department of Materials and Metallurgical Engineering, BUET; and Bangladesh Council of Scientific and Industrial Research (BCSIR), Dhaka for their assistance with synthesis and characterization.

References

1 M. R. Siddiki, S. A. Abtahee, M. Hasan, M. Rahaman, M. R. Islam and M. A. Zubair, Defect mediated modulation of electrochemical efficacy and stability of Fe_3O_4 nanodiamond incorporated MoS_2 based hierarchical 2D nanostructures for high performance supercapacitor electrodes, *Mater. Adv.*, 2025, **6**, 5126.

2 N. Choudhary, M. R. Islam, N. Kang, L. Tetard, Y. Jung and S. I. Khondaker, Two-dimensional lateral heterojunction through bandgap engineering of MoS_2 via oxygen plasma, *J. Phys.: Condens. Matter*, 2016, **28**, 364002.

3 R. Islam Md, M. Rahaman, M. Billah Md and M. R. Islam, Hydrothermal synthesis of an MoS_2/MnO_2 nanocomposite: a unique 3D-nanoflower/1D-nanorod structure for high-performance energy storage applications, *Mater. Adv.*, 2024, **5**, 5307–5321.

4 A. G. Olabi, T. Wilberforce, M. Ramadan, M. A. Abdelkareem and A. H. Alami, Compressed air energy storage systems: Components and operating parameters – A review, *J. Energy Storage*, 2021, **34**, 102000.

5 S. Wang, B. Y. Guan, L. Yu and X. W. Lou (David), Rational Design of Three-Layered TiO_2@Carbon@MoS_2 Hierarchical

Nanotubes for Enhanced Lithium Storage, *Adv. Mater.*, 2017, **29**, 1702724.
6 A. M. Abraham, S. P. Lonkar, V. V. Pillai and S. M. Alhassan, Three-Dimensional MoS_2 Nanodot-Impregnated Nickel Foam Electrodes for High-Performance Supercapacitor Applications, *ACS Omega*, 2020, **5**, 11721–11729.
7 E. Pomerantseva and Y. Gogotsi, Two-dimensional heterostructures for energy storage, *Nat. Energy*, 2017, **2**, 17089.
8 Z. A. Hrbe and S. W. Hashim, Tungsten disulfide-nickel oxide hybrids as high-performance supercapacitors, *J. Met. Mater. Miner.*, 2022, **32**, 86–92.
9 M. U. Khalid, S. Zulfiqar, M. N. Khan, I. Shakir, M. F. Warsi and E. W. Cochran, Electrochemical performance enhancement of MnO_2 nanowires through silver incorporation for next-generation supercapacitors, *Mater. Adv.*, 2024, **5**, 6170–6184.
10 D. Wu, X. Xie, Y. Zhang, D. Zhang, W. Du, X. Zhang and B. Wang, MnO_2/Carbon Composites for Supercapacitor: Synthesis and Electrochemical Performance, *Front. Mater.*, 2020, **7**, 2.
11 X. Zhou, F. Sun, C. Zhang and C. Sun, Stochastically predictive co-optimization of the speed planning and powertrain controls for electric vehicles driving in random traffic environment safely and efficiently, *J. Power Sources*, 2022, **528**, 231200.
12 G. Srivastava, Ravina, S. Dalela, N. K. Gautam, S. Kumar, S. Z. Hashmi, M. A. Ahmad, A. M. Quraishi, V. Khanna and P. A. Alvi, Synthesis and characterizations of MnO_2/CNT nanocomposite for usage as electrodes in high-performance supercapacitor, *Nano Trends*, 2025, **9**, 100067.
13 S. Simon, L. V. Theresa and S. P. B., Unzipped MWCNT/polypyrrole hybrid composites: a pathway to high-performance asymmetric supercapacitors, *Mater. Adv.*, 2025, **6**, 2002–2015.
14 M. Rana, V. Sai Avvaru, N. Boaretto, V. A. De La Peña O'Shea, R. Marcilla, V. Etacheri and J. J. Vilatela, High rate hybrid MnO_2@CNT fabric anodes for Li-ion batteries: properties and a lithium storage mechanism study by *in situ* synchrotron X-ray scattering, *J. Mater. Chem. A*, 2019, **7**, 26596–26606.
15 L. Lu, S. Xu, J. An and S. Yan, Electrochemical performance of CNTs/RGO/MnO_2 composite material for supercapacitor, *Nanomater. Nanotechnol.*, 2016, **6**, 184798041666368.
16 Y. Li, Y. Sun, S. Zhang, X. Wu, M. Song, M. Jiao, Q. Qin and L. Mi, Self-assembled molybdenum disulfide nanoflowers regulated by lithium sulfate for high performance supercapacitors, *RSC Adv.*, 2023, **13**, 26509–26515.
17 J. Liu, B. Yuan, D. Chen, L. Dong, H. Xie, S. Zhong, Y. Ji, Y. Liu, J. Han, C. Yang and W. He, Pseudocapacitance and diffusion-controlled dual modes of MoS_2 nano-particles enable high long-cycle anode capacity, *Chem. Eng. J. Adv.*, 2023, **14**, 100470.
18 Z. Ping, L. Junjie and L. Yunchun, Optimization of the electrodeposition process of a polypyrrole/multi-walled carbon nanotube fiber electrode for a flexible supercapacitor, *RSC Adv.*, 2022, **12**, 18134–18143.
19 R. Perez-Gonzalez, Z. Peng, D. Camacho, A. I. Oliva, Q. Pei, A. Zakhidov, A. Encinas and J. Oliva, All solid state stretchable carbon nanotube based supercapacitors with controllable output voltage, *J. Energy Storage*, 2020, **32**, 101844.
20 N. Poirot, V. Rajalingam, R. N. Murgu, R. Omnée and E. Raymundo-Piñero, Nanotexturing TiO_2 over carbon nanotubes for high-energy and high-power density pseudocapacitors in organic electrolytes, *Front. Mater.*, 2022, **9**, 1083191.
21 X. Chen, J. Ding, J. Jiang, G. Zhuang, Z. Zhang and P. Yang, Preparation of a MoS_2/carbon nanotube composite as an electrode material for high-performance supercapacitors, *RSC Adv.*, 2018, **8**, 29488–29494.
22 D. Sahoo, J. Shakya, N. Ali, W. J. Yoo and B. Kaviraj, Edge Rich Ultrathin Layered MoS_2 Nanostructures for Superior Visible Light Photocatalytic Activity, *Langmuir*, 2022, **38**, 1578.
23 H. Ganesha, S. Veeresh, Y. S. Nagaraju, M. Vandana, M. Basappa, H. Vijeth and H. Devendrappa, 2-Dimensional layered molybdenum disulfide nanosheets and CTAB-assisted molybdenum disulfide nanoflower for high performance supercapacitor application, *Nanoscale Adv.*, 2022, **4**, 521–531.
24 N. Kumar, K. G. Prasad, A. Sen and T. Maiyalagan, Enhanced pseudocapacitance from finely ordered pristine alpha-MnO_2 nanorods at favourably high current density using redox additive, *Appl. Surf. Sci.*, 2018, **449**, 492–499.
25 D. Sahoo, J. Shakya, S. Choudhury, S. S. Roy, L. Devi, B. Singh, S. Ghosh and B. Kaviraj, High-Performance MnO_2 Nanowire/MoS_2 Nanosheet Composite for a Symmetrical Solid-State Supercapacitor, *ACS Omega*, 2022, **7**, 16895–16905.
26 Z. Zhou, Y. Lin, P. Zhang, E. Ashalley, M. Shafa, H. Li, J. Wu and Z. Wang, Hydrothermal fabrication of porous MoS_2 and its visible light photocatalytic properties, *Mater. Lett.*, 2014, **131**, 122–124.
27 G. Feng, A. Wei, Y. Zhao and J. Liu, Synthesis of flower-like MoS_2 nanosheets microspheres by hydrothermal method, *J. Mater. Sci.: Mater. Electron.*, 2015, **26**, 8160–8166.
28 L. Zaraska, G. D. Sulka, J. Szeremeta and M. Jaskuła, Porous anodic alumina formed by anodization of aluminum alloy (AA1050) and high purity aluminum, *Electrochim. Acta*, 2010, **55**, 4377–4386.
29 L. A. Piankova, N. A. Malakhova, N. Y. Stozhko, Z. Brainina Kh, A. M. Murzakaev and O. R. Timoshenkova, Bismuth nanoparticles in adsorptive stripping voltammetry of nickel, *Electrochem. Commun.*, 2011, **13**, 981–984.
30 H. Ahmad Md, R. B. Alam, A. Ul-hamid, S. F. U. Farhad and M. R. Islam, Hydrothermal synthesis of Co_3O_4 nanoparticles decorated three dimensional MoS_2 nanoflower for exceptionally stable supercapacitor electrode with improved capacitive performance, *J. Energy Storage*, 2022, **47**, 103551.
31 P. Korusenko, K. Kharisova, E. Knyazev, O. Levin, A. Vinogradov and E. Alekseeva, Surface Engineering of Multi-Walled Carbon Nanotubes via Ion-Beam Doping: Pyridinic and Pyrrolic Nitrogen Defect Formation, *Appl. Sci.*, 2023, **13**, 11057.
32 N. M. Nurazzi, F. A. Sabaruddin, M. M. Harussani, S. H. Kamarudin, M. Rayung, M. R. M. Asyraf, H. A. Aisyah,

M. N. F. Norrrahim, R. A. Ilyas, N. Abdullah, E. S. Zainudin, S. M. Sapuan and A. Khalina, Mechanical Performance and Applications of CNTs Reinforced Polymer Composites—A Review, *Nanomaterials*, 2021, **11**, 2186.

33 X. Wang and Y. Li, Synthesis and Formation Mechanism of Manganese Dioxide Nanowires/Nanorods, *Chem. – Eur. J.*, 2003, **9**, 300–306.

34 X. Sun, J. Dai, Y. Guo, C. Wu, F. Hu, J. Zhao, X. Zeng and Y. Xie, Semimetallic molybdenum disulfide ultrathin nanosheets as an efficient electrocatalyst for hydrogen evolution, *Nanoscale*, 2014, **6**, 8359–8367.

35 H. Nolan, N. McEvoy, M. O'Brien, N. C. Berner, C. Yim, T. Hallam, A. R. McDonald and G. S. Duesberg, Molybdenum disulfide/pyrolytic carbon hybrid electrodes for scalable hydrogen evolution, *Nanoscale*, 2014, **6**, 8185.

36 J. Ihli, J. N. Clark, A. S. Côté, Y.-Y. Kim, A. S. Schenk, A. N. Kulak, T. P. Comyn, O. Chammas, R. J. Harder, D. M. Duffy, I. K. Robinson and F. C. Meldrum, Strain-relief by single dislocation loops in calcite crystals grown on self-assembled monolayers, *Nat. Commun.*, 2016, **7**, 11878.

37 J. Shahbaz, M. R. Khawar, S. Jang, N. A. Shad, A. Ahmad, M. D. Albaqami, U. Zahid, K. Y. Rhee, Y. Javed and D. Choi, A hierarchical surface-coated 3D-nanoflower network of MoS_2 with abundant reaction sites for high-performance asymmetric supercapacitor, *J. Alloys Compd.*, 2025, **1010**, 177230.

38 F. Liang, J. Yu, J. Chen, D. Wang, C. Lin, C. Zhu, M. Wang, L. Dong and C. Li, A novel boron-based ionic liquid electrolyte for high voltage lithium-ion batteries with outstanding cycling stability, *Electrochim. Acta*, 2018, **283**, 111–120.

39 Q. Wang, Y. Wu, X. Deng, L. Xiang, K. Xu, Y. Li and Y. Xie, Preparation and Bolometric Responses of MoS_2 Nanoflowers and Multi-Walled Carbon Nanotube Composite Network, *Nanomaterials*, 2022, **12**, 495.

40 L. Hu, Y. Ren, H. Yang and Q. Xu, Fabrication of 3D Hierarchical MoS_2/Polyaniline and MoS_2/C Architectures for Lithium-Ion Battery Applications, *ACS Appl. Mater. Interfaces*, 2014, **6**, 14644–14652.

41 F. Pan, J. Wang, Z. Yang, L. Gu and Y. Yu, MoS_2 –graphene nanosheet–CNT hybrids with excellent electrochemical performances for lithium-ion batteries, *RSC Adv.*, 2015, **5**, 77518–77526.

42 C. Tsai, H. Li, S. Park, J. Park, H. S. Han, J. K. Nørskov, X. Zheng and F. Abild-Pedersen, Electrochemical generation of sulfur vacancies in the basal plane of MoS_2 for hydrogen evolution, *Nat. Commun.*, 2017, **8**, 15113.

43 M. I. Alam, R. Sumichika, J. Tsuchimoto, T. Komeda and A. Teramoto, Interface analysis of oxide free MoS_2 films fabricated by solution process, *Sci. Rep.*, 2024, **14**, 26779.

44 L. A. H. Jones, Z. Xing, J. E. N. Swallow, H. Shiel, T. J. Featherstone, M. J. Smiles, N. Fleck, P. K. Thakur, T.-L. Lee, L. J. Hardwick, D. O. Scanlon, A. Regoutz, T. D. Veal and V. R. Dhanak, Band Alignments, Electronic Structure, and Core-Level Spectra of Bulk Molybdenum Dichalcogenides (MoS_2, $MoSe_2$, and $MoTe_2$), *J. Phys. Chem. C*, 2022, **126**, 21022–21033.

45 M.-H. Chiu, C. Zhang, H.-W. Shiu, C.-P. Chuu, C.-H. Chen, C.-Y. S. Chang, C.-H. Chen, M.-Y. Chou, C.-K. Shih and L.-J. Li, Determination of band alignment in the single-layer MoS_2/WSe_2 heterojunction, *Nat. Commun.*, 2015, **6**, 7666.

46 M. H. Azarian, S. Nijpanich, N. Chanlek and W. Sutapun, Probing capping mechanisms and polymer matrix loading of biogenic vaterite $CaCO_3$–Ag hybrid through X-ray photoelectron spectroscopy (XPS), *RSC Adv.*, 2024, **14**, 14624–14639.

47 R. Amin, A. Hossain Md and Y. Zakaria, Interfacial Kinetics and Ionic Diffusivity of the Electrodeposited MoS_2 Film, *ACS Appl. Mater. Interfaces*, 2018, **10**, 13509–13518.

48 E. Vernickaitė, M. Lelis, N. Tsyntsaru, V. Pakštas and H. Cesiulis, XPS studies on the Mo oxide-based coatings electrodeposited from highly saturated acetate bath, *Chemija*, 2020, **31**, 203–209.

49 B. Li, L. Jiang, X. Li, P. Ran, P. Zuo, A. Wang, L. Qu, Y. Zhao, Z. Cheng and Y. Lu, Preparation of Monolayer MoS_2 Quantum Dots using Temporally Shaped Femtosecond Laser Ablation of Bulk MoS_2 Targets in Water, *Sci. Rep.*, 2017, **7**, 11182.

50 A. Bayou, B. Asbani, Y. Doubi, N. Rajput, A. Campos, M. El Marssi and M. Jouiad, Superior photoelectrochemical performance of electrodeposited 1T/2H–MoS_2 quantum dots for hydrogen evolution, *Int. J. Hydrogen Energy*, 2025, **139**, 107–115.

51 S. Chromik, A. Rosová, E. Dobročka, A. P. Kobzev, M. Hulman, M. Sojkova, P. Hutár and D. Machajdík, *MoS_2 thin films prepared by sulfurization Nanoengineering: Fabrication, Properties, Optics, and Devices XIV Nanoengineering: Fabrication, Properties, Optics, and Devices XIV*, ed. E. M. Campo, E. A. Dobisz and L. A. Eldada, SPIE, San Diego, United States, 2017, vol. 10354, p. 56.

52 Y. Du, Z. Hua, W. Huang, M. Wu, M. Wang, J. Wang, X. Cui, L. Zhang, H. Chen and J. Shi, Mesostructured amorphous manganese oxides: facile synthesis and highly durable elimination of low-concentration NO at room temperature in air, *Chem. Commun.*, 2015, **51**, 5887–5889.

53 R. Gostynski, J. Conradie and E. Erasmus, Significance of the electron-density of molecular fragments on the properties of manganese(iii) β-diketonato complexes: an XPS and DFT study, *RSC Adv.*, 2017, **7**, 27718–27728.

54 V. Tsurkan, M. Demeter, B. Schneider, D. Hartmann and M. Neumann, Exchange splitting of the Cr, Fe and Mn 3s XPS spectra in some ternary magnetic semiconductor sulphides, *Solid State Commun.*, 2000, **114**, 149–154.

55 E. S. Ilton, J. E. Post, P. J. Heaney, F. T. Ling and S. N. Kerisit, XPS determination of Mn oxidation states in Mn (hydr)oxides, *Appl. Surf. Sci.*, 2016, **366**, 475–485.

56 K. C. Lalithambika, K. Shanmugapriya and S. Sriram, Photocatalytic activity of MoS_2 nanoparticles: an experimental and DFT analysis, *Appl. Phys. A: Mater. Sci. Process.*, 2019, **125**, 817.

57 N. H. Tran, M. A. Wilson, A. S. Milev, J. R. Bartlett, R. N. Lamb, D. Martin and G. S. K. Kannangara, Photoemission and absorption spectroscopy of carbon nanotube interfacial interaction, *Adv. Colloid Interface Sci.*, 2009, **145**, 23–41.

58 M. C. Biesinger, Accessing the robustness of adventitious carbon for charge referencing (correction) purposes in XPS analysis: Insights from a multi-user facility data review, *Appl. Surf. Sci.*, 2022, **597**, 153681.
59 H. Estrade-Szwarckopf, XPS photoemission in carbonaceous materials: A ''defect'' peak beside the graphitic asymmetric peak, *Carbon*, 2004, **42**, 1713–1721.
60 S. Hasan, A. H. Reaz, S. Das, C. K. Roy and M. A. Basith, $CuCo_2S_4$–MoS_2 nanocomposite: a novel electrode for high-performance supercapacitors, *J. Mater. Chem. C*, 2022, **10**, 7980–7996.
61 M. Gaire, K. Liang, S. Luo, B. Subedi, S. Adireddy, K. Schroder, S. Farnsworth and D. B. Chrisey, Nanostructured manganese oxides electrode with ultra-long lifetime for electrochemical capacitors, *RSC Adv.*, 2020, **10**, 16817–16825.
62 V. T. Nguyen, F. N. I. Sari and J.-M. Ting, 3D hierarchical cobalt vanadate nanosheet arrays on Ni foam coupled with redox additive for enhanced supercapacitor performance, *RSC Adv.*, 2022, **12**, 29170–29176.
63 V. H. Nguyen, C. Lamiel and J.-J. Shim, Mesoporous 3D graphene@$NiCo_2O_4$ arrays on nickel foam as electrodes for high-performance supercapacitors, *Mater. Lett.*, 2016, **170**, 105–109.
64 J. Stepiński and S. Angielski, Bicarbonate inhibition of rat kidney aconitate hydratase isoenzymes, *Curr. Probl. Clin. Biochem.*, 1975, **4**, 65–69.
65 T. Kahn, J. Bosch, M. F. Levitt and M. H. Goldstein, Effect of sodium nitrate loading on electrolyte transport by the renal tubule, *Am. J. Physiol.*, 1975, **229**, 746–753.
66 E. Rafiee, M. Farzam, M. A. Golozar and A. Ashrafi, An Investigation on Dislocation Density in Cold-Rolled Copper Using Electrochemical Impedance Spectroscopy, *ISRN Corros*, 2013, **2013**, 1–6.
67 P. S. Chen, Y. Hu, S.-Y. Li, M. Mazurkiewicz-Pawlicka and A. Małolepszy, Preparation of a MoS_2/carbon nanotube nanocomposite by hydrothermal method for supercapacitor, *Int. J. Electrochem. Sci.*, 2024, **19**, 100523.
68 N. Wu, X. Bai, D. Pan, B. Dong, R. Wei, N. Naik, R. R. Patil and Z. Guo, Recent Advances of Asymmetric Supercapacitors, *Adv. Mater. Interfaces*, 2021, **8**, 2001710.
69 Y. Lin, C. Lian, M. U. Berrueta, H. Liu and R. Van Roij, Microscopic Model for Cyclic Voltammetry of Porous Electrodes, *Phys. Rev. Lett.*, 2022, **128**, 206001.
70 A. Abdulhameed, N. Z. A. Wahab, M. N. Mohtar, M. N. Hamidon, S. Shafie and I. A. Halin, Methods and Applications of Electrical Conductivity Enhancement of Materials Using Carbon Nanotubes, *J. Electron. Mater.*, 2021, **50**, 3207–3221.
71 Y. Wang, X. Wang, X. Li, Y. Bai, H. Xiao, R. Liu and G. Yuan, Construction of MoS_2/MnO_2 nanosheets on carbon nanotubes for high-performance supercapacitor electrodes, *J. Mater. Chem. A*, 2021, **9**, 9842–9852.
72 G. A. Tafete, G. Thothadri and M. K. Abera, A review on carbon nanotube-based composites for electrocatalyst applications, *Fuller. Nanotub. Carbon Nanostructures*, 2022, **30**, 1075–1083.
73 J. B. Cook, H. Kim, Y. Yan, J. S. Ko, S. Robbennolt, B. Dunn and S. H. Tolbert, Mesoporous MoS_2 as a Transition Metal Dichalcogenide Exhibiting Pseudocapacitive Li and Na-Ion Charge Storage, *Adv. Energy Mater.*, 2016, **6**, 1501937.
74 W.-S. Li, M.-L. Chang, K.-C. Chuang, Y.-S. Li, J.-D. Luo and H.-C. Cheng, Electrochemical Properties of CNT/MnO_2 Hybrid Nanostructure with Low-Temperature Hydrothermal Synthesis as High-Performance Supercapacitor, *J. Electrochem. Soc.*, 2019, **166**, A2194–A2198.
75 B. Bhujun, M. T. T. Tan and A. S. Shanmugam, Study of mixed ternary transition metal ferrites as potential electrodes for supercapacitor applications, *Results Phys.*, 2017, **7**, 345–353.
76 Y. Xie and H. Du, Electrochemical capacitance of a carbon quantum dots–polypyrrole/titania nanotube hybrid, *RSC Adv.*, 2015, **5**, 89689–89697.
77 L. Hu, W. Chen, X. Xie, N. Liu, Y. Yang, H. Wu, Y. Yao, M. Pasta, H. N. Alshareef and Y. Cui, Symmetrical MnO_2 –Carbon Nanotube–Textile Nanostructures for Wearable Pseudocapacitors with High Mass Loading, *ACS Nano*, 2011, **5**, 8904–8913.
78 X.-L. Han, J. Zhang, Z.-S. Wang, H. A. Younus and D.-W. Wang, Engineering the microstructures of manganese dioxide coupled with oxygen vacancies for boosting aqueous ammonium-ion storage in hybrid capacitors, *Rare Met.*, 2024, **43**, 5734–5746.
79 K. Singh, S. Kumar, K. Agarwal, K. Soni, V. Ramana Gedela and K. Ghosh, Three-dimensional Graphene with MoS_2 Nanohybrid as Potential Energy Storage/Transfer Device, *Sci. Rep.*, 2017, **7**, 9458.
80 L. Chen, X. Zhang, Z. Wang, X. Kong, J. Zhang, J. Zeng and D. Wang, Layered $V_{10}O_{24}{\cdot}nH_2O$ as a new ammonium ion host material for aqueous and quasi-solid-state ammonium-ion hybrid capacitors, *Chem. Eng. J.*, 2024, **500**, 157472.
81 H. Peçenek, S. Yetiman, F. K. Dokan, M. S. Onses, E. Yılmaz and E. Sahmetlioglu, Effects of carbon nanomaterials and MXene addition on the performance of nitrogen doped MnO_2 based supercapacitors, *Ceram. Int.*, 2022, **48**, 7253–7260.
82 R. Singhal, T. Sadowski, M. Chaudhary, R. V. Tucci, J. Scanley, R. Patel, P. Kumar Patel, S. Gagnon, A. Koni, K. Singhal, P. K. LeMaire, R. Kumar Sharma, B. P. Singh and C. C. Broadbridge, Optimization of manganese dioxide-multiwall carbon nanotube composite electrodes for supercapacitor applications, *Mater. Sci. Energy Technol.*, 2024, **7**, 228–236.
83 A. Bardin, V. Ignatjev, A. Orlov and S. Perchenko, Verifying of reciprocal relations for nonlinear quadripole in unsteady mode, *Results Phys.*, 2017, **7**, 665–666.
84 M. Szkoda, A. Ilnicka, K. Trzciński, Z. Zarach, D. Roda and A. P. Nowak, Synthesis and characterization of MoS_2-carbon based materials for enhanced energy storage applications, *Sci. Rep.*, 2024, **14**, 26128.
85 X. Chen, S. M. Shinde, K. P. Dhakal, S. W. Lee, H. Kim, Z. Lee and J.-H. Ahn, Degradation behaviors and mechanisms of MoS_2 crystals relevant to bioabsorbable electronics, *NPG Asia Mater.*, 2018, **10**, 810–820.

86 Z. Wang, Z. Li, J. Feng, S. Yan, W. Luo, J. Liu, T. Yu and Z. Zou, MnO_2 nanolayers on highly conductive $TiO_{0.54}N_{0.46}$ nanotubes for supercapacitor electrodes with high power density and cyclic stability, *Phys. Chem. Chem. Phys.*, 2014, **16**, 8521.

87 H. Wang, X. Xu and A. Neville, Facile synthesis of vacancy-induced 2H-MoS_2 nanosheets and defect investigation for supercapacitor application, *RSC Adv.*, 2021, **11**, 26273–26283.

88 J. S. Bulmer, A. Kaniyoor and J. A. Elliott, A Meta-Analysis of Conductive and Strong Carbon Nanotube Materials, *Adv. Mater.*, 2021, **33**, 2008432.

89 E. Inci Yesilyurt, J. Pionteck, F. Simon and B. Voit, Fabrication of PANI/MWCNT supercapacitors based on a chitosan binder and aqueous electrolyte for enhanced energy storage, *RSC Appl. Polym.*, 2023, **1**, 97–110.

90 B. Yenigun, M. S. Chaudhry, E. Gkouti and A. Czekanski, Characterization of Mode I and Mode II Interlaminar Fracture Toughness in CNT-Enhanced CFRP under Various Temperature and Loading Rates, *Nanomaterials*, 2023, **13**, 1729.

91 M. M. Baig, E. Pervaiz, M. Yang and I. H. Gul, High-Performance Supercapacitor Electrode Obtained by Directly Bonding 2D Materials: Hierarchal MoS_2 on Reduced Graphene Oxide, *Front. Mater.*, 2020, **7**, 88.

92 F. Wang, G. Li, J. Zheng, J. Ma, C. Yang and Q. Wang, Hydrothermal synthesis of flower-like molybdenum disulfide microspheres and their application in electrochemical supercapacitors, *RSC Adv.*, 2018, **8**, 38945–38954.

93 M. Chen, Y. Dai, J. Wang, Q. Wang, Y. Wang, X. Cheng and X. Yan, Smart combination of three-dimensional-flower-like MoS_2 nanospheres/interconnected carbon nanotubes for application in supercapacitor with enhanced electrochemical performance, *J. Alloys Compd.*, 2017, **696**, 900–906.

94 X. Bi, X. Wang, X. Shen, H. Yu, X. Zhang and J. Bai, Ethanol Molecule Engineering Toward Stabilized 1T-MoS_2 with Extraordinary Sodium Storage Performance, *Molecules*, 2025, **30**, 3801.

95 L. Huang, X. Luo, C. Chen and Q. Jiang, A high specific capacity aqueous zinc-manganese battery with a ε-MnO_2 cathode, *Ionics*, 2021, **27**, 3933–3941.